

---

# Analysis of Shock and High-Rate Data for Ceramics: Equation of State Properties and Fragmentation in the Ballistic Environment

## Report

by  
Dennis E. Grady

Prepared for  
U.S. Army TARDEC  
Emerging Technologies Team

May 2009

Contract No. W56HZV-08-P-L594

ARA Project No. L18637

**Applied Research Associates, Inc.**  
4300 San Mateo Blvd. NE, Suite A-220  
Albuquerque, New Mexico 87110  
(505) 883-3636



<b>REPORT DOCUMENTATION PAGE</b>					<i>Form Approved OMB No. 0704-0188</i>	
The public reporting burden for this collection of information is estimated to average 1 hour per response, including the time for reviewing instructions, searching existing data sources, gathering and maintaining the data needed, and completing and reviewing the collection of information. Send comments regarding this burden estimate or any other aspect of this collection of information, including suggestions for reducing the burden, to Department of Defense, Washington Headquarters Services, Directorate for Information Operations and Reports (0704-0188), 1215 Jefferson Davis Highway, Suite 1204, Arlington, VA 22202-4302. Respondents should be aware that notwithstanding any other provision of law, no person shall be subject to any penalty for failing to comply with a collection of information if it does not display a currently valid OMB control number.						
<b>PLEASE DO NOT RETURN YOUR FORM TO THE ABOVE ADDRESS.</b>						
<b>1. REPORT DATE (DD-MM-YYYY)</b> 05/01/2009		<b>2. REPORT TYPE</b> FINAL			<b>3. DATES COVERED (From - To)</b> 06/12/2009-06/11/2009	
<b>4. TITLE AND SUBTITLE</b> Analysis of Shock and High-Rate Data for Ceramics: Equation of State Properties and Fragmentation in the Ballistic Environment.					<b>5a. CONTRACT NUMBER</b> W56HZV-07-P-L618	
					<b>5b. GRANT NUMBER</b>	
					<b>5c. PROGRAM ELEMENT NUMBER</b>	
					<b>5d. PROJECT NUMBER</b>	
<b>6. AUTHOR(S)</b> Dr. Dennis E. Grady					<b>5e. TASK NUMBER</b>	
					<b>5f. WORK UNIT NUMBER</b>	
<b>7. PERFORMING ORGANIZATION NAME(S) AND ADDRESS(ES)</b> Applied Research Associates, Inc. 4300 San Mateo Blvd., Suite A-220 Albuquerque, NM 87110					<b>8. PERFORMING ORGANIZATION REPORT NUMBER</b> ARA Project No. L18637	
<b>9. SPONSORING/MONITORING AGENCY NAME(S) AND ADDRESS(ES)</b> TACOM LCMC 6501 E. 11 Mile Road Warren, MI 48397-5000					<b>10. SPONSOR/MONITOR'S ACRONYM(S)</b>	
					<b>11. SPONSOR/MONITOR'S REPORT NUMBER(S)</b>	
<b>12. DISTRIBUTION/AVAILABILITY STATEMENT</b> Approved for public release; distribution is unlimited						
<b>13. SUPPLEMENTARY NOTES</b>						
<b>14. ABSTRACT</b> <p>The project effort reported on here is a continuing study undertaken to collect, survey, analyze and model shock wave, and other related high-rate and supporting data, available for candidate armor ceramics with emphasis on response in the ballistic environment. Ceramics considered here include the various light metal-nonmetal compounds selected by the Army for consideration such as silicon carbide and aluminum oxide, as well as other ceramics, glass ceramics and glasses currently being pursued by TARDEC with high potential for armor applications.</p> <p>The TARDEC/Army Research Laboratories program in armor ceramics currently involves a number of efforts at various facilities including materials research, experimental studies and computational modeling. Thus, the present effort focuses on available data, analysis approaches and theoretical concepts, not currently under consideration at other laboratories, which best complements and furthers goals of the current TARDEC program.</p>						
<b>15. SUBJECT TERMS</b>						
<b>16. SECURITY CLASSIFICATION OF:</b>			<b>17. LIMITATION OF ABSTRACT</b>  UU	<b>18. NUMBER OF PAGES</b>  58	<b>19a. NAME OF RESPONSIBLE PERSON</b> Dr. Dennis E. Grady	
a. REPORT  UU	b. ABSTRACT  UU	c. THIS PAGE  UU			<b>19b. TELEPHONE NUMBER (Include area code)</b> (505) 883-3636	

## INSTRUCTIONS FOR COMPLETING SF 298

**1. REPORT DATE.** Full publication date, including day, month, if available. Must cite at least the year and be Year 2000 compliant, e.g. 30-06-1998; xx-06-1998; xx-xx-1998.

**2. REPORT TYPE.** State the type of report, such as final, technical, interim, memorandum, master's thesis, progress, quarterly, research, special, group study, etc.

**3. DATES COVERED.** Indicate the time during which the work was performed and the report was written, e.g., Jun 1997 - Jun 1998; 1-10 Jun 1996; May - Nov 1998; Nov 1998.

**4. TITLE.** Enter title and subtitle with volume number and part number, if applicable. On classified documents, enter the title classification in parentheses.

**5a. CONTRACT NUMBER.** Enter all contract numbers as they appear in the report, e.g. F33615-86-C-5169.

**5b. GRANT NUMBER.** Enter all grant numbers as they appear in the report, e.g. AFOSR-82-1234.

**5c. PROGRAM ELEMENT NUMBER.** Enter all program element numbers as they appear in the report, e.g. 61101A.

**5d. PROJECT NUMBER.** Enter all project numbers as they appear in the report, e.g. 1F665702D1257; ILIR.

**5e. TASK NUMBER.** Enter all task numbers as they appear in the report, e.g. 05; RF0330201; T4112.

**5f. WORK UNIT NUMBER.** Enter all work unit numbers as they appear in the report, e.g. 001; AFAPL30480105.

**6. AUTHOR(S).** Enter name(s) of person(s) responsible for writing the report, performing the research, or credited with the content of the report. The form of entry is the last name, first name, middle initial, and additional qualifiers separated by commas, e.g. Smith, Richard, J, Jr.

**7. PERFORMING ORGANIZATION NAME(S) AND ADDRESS(ES).** Self-explanatory.

**8. PERFORMING ORGANIZATION REPORT NUMBER.** Enter all unique alphanumeric report numbers assigned by the performing organization, e.g. BRL-1234; AFWL-TR-85-4017-Vol-21-PT-2.

**9. SPONSORING/MONITORING AGENCY NAME(S) AND ADDRESS(ES).** Enter the name and address of the organization(s) financially responsible for and monitoring the work.

**10. SPONSOR/MONITOR'S ACRONYM(S).** Enter, if available, e.g. BRL, ARDEC, NADC.

**11. SPONSOR/MONITOR'S REPORT NUMBER(S).** Enter report number as assigned by the sponsoring/monitoring agency, if available, e.g. BRL-TR-829; -215.

**12. DISTRIBUTION/AVAILABILITY STATEMENT.** Use agency-mandated availability statements to indicate the public availability or distribution limitations of the report. If additional limitations/ restrictions or special markings are indicated, follow agency authorization procedures, e.g. RD/FRD, PROPIN, ITAR, etc. Include copyright information.

**13. SUPPLEMENTARY NOTES.** Enter information not included elsewhere such as: prepared in cooperation with; translation of; report supersedes; old edition number, etc.

**14. ABSTRACT.** A brief (approximately 200 words) factual summary of the most significant information.

**15. SUBJECT TERMS.** Key words or phrases identifying major concepts in the report.

**16. SECURITY CLASSIFICATION.** Enter security classification in accordance with security classification regulations, e.g. U, C, S, etc. If this form contains classified information, stamp classification level on the top and bottom of this page.

**17. LIMITATION OF ABSTRACT.** This block must be completed to assign a distribution limitation to the abstract. Enter UU (Unclassified Unlimited) or SAR (Same as Report). An entry in this block is necessary if the abstract is to be limited.

---

## Acknowledgments

The author wishes to thank attendees of the several meetings hosted during this program year, on topics of ceramic armor materials testing and development, for providing stimulus for the work reported here. In particular, the author thanks Lisa Prokurat-Franks, Douglas Templeton, Timothy Holmquist, Gordon Johnson, Datta Dandekar, Murli Mangnani, Xin Sun, Charlie Anderson, Dennis Orphal and Andrew Wereszczak for their respective incentives and input.

The author also wishes to thank Tracy Vogler and Scott Alexander at Sandia National Laboratories for continuing discussions on topics of this report and Craig Doolittle and Terry Caipen at Applied Research Associates for technical help on several parts of the report. Partial support for the present research was also provided by Sandia National Laboratories through the DOE/DOD MOU Munitions Technology Development Program.

# Table of Contents

<b>I</b>	<b>Introduction and Summary .....</b>	<b>1</b>
	Introduction .....	1
	Summary .....	2
<b>II</b>	<b>Background.....</b>	<b>5</b>
<b>III</b>	<b>Tungsten Carbide Ceramic EOS and Strength.....</b>	<b>7</b>
	Tungsten Carbide Ceramic and Composition Effects .....	7
	Tungsten Carbide Materials.....	8
	Hugoniot Properties of Tungsten Carbide Ceramics.....	9
	Hydrodynamic Response.....	9
	Static High-Pressure and Shock Hugoniot Compression EOS .....	11
	Ultrasonic EOS .....	13
	X-Ray Diffraction Compressibility .....	14
	Dynamic Strength and Composition .....	17
<b>IV</b>	<b>Boron Carbide Ceramic EOS and Strength .....</b>	<b>19</b>
	Phase Transformation from Shock Hugoniot Data.....	20
	Hydrodynamic Equation of State .....	25
	Strength Under Shock Compression and Static Scaling Studies .....	27
<b>V</b>	<b>Fragmentation in the Ballistic Event.....</b>	<b>31</b>
	Fragmentation Ductile and Brittle Solids.....	31
	Mott Fragmentation .....	32
	Brittle Fragmentation .....	33
	Equilibrium Fragmentation.....	34
	Nonequilibrium (Brittle) Fragmentation .....	39
	Status of Brittle Fragmentation Theory .....	46
	Fragmentation in Edge-On Plate Impact.....	46
	Modelling the Impact Failure Event .....	47
	Comparisons with Impact Failure .....	50
<b>VII</b>	<b>Closure .....</b>	<b>53</b>

**VIII References ..... 55**

# I Introduction and Summary

The U.S. Army is considering high quality ceramics and glass ceramics prepared from light metal-nonmetal compounds as engineering materials for armoring vehicles against kinetic energy threats. Application of ceramics within armor systems requires a full understanding of the physical and mechanical response of ceramics to the range of impact and penetration conditions of concern. The present report documents continued work in support of the TARDEC/ARL efforts on this topic.

## *Introduction*

The project effort reported on here is a continuing study undertaken to collect, survey, analyze and model shock wave, and other related high-rate and supporting data, available for candidate armor ceramics with emphasis on response in the ballistic environment. Ceramics considered here include the various light metal-nonmetal compounds selected by the Army for consideration such as silicon carbide and aluminum oxide, as well as other ceramics, glass ceramics and glasses currently being pursued by TARDEC with high potential for armor applications.

The TARDEC/Army Research Laboratories program in armor ceramics currently involves a number of efforts at various facilities including materials research, experimental studies and computational modeling. Thus, the present effort focuses on available data, analysis approaches and theoretical concepts, not currently under consideration at other laboratories, which best complements and furthers goals of the current TARDEC program.

The present effort also includes physics-based modeling of the response of ceramics and glasses under impact and penetration for purposes of furthering computational modeling of ceramics in armor applications. This supporting theoretical effort serves both the furthering of computational models, and the analysis and interpretation of data necessary to benchmark the models. Both objectives fall within the tasks of the present project.

The present year's efforts are focused on both the assessment of shock wave and related experimental data, and on theoretical material response modeling. The purpose is for furthering computational modeling and simulation of ceramics in ballistic applications.

Shock equation of state (EOS) and strength data for tungsten carbide and boron carbide ceramics are surveyed to provide the best available assessment of the data for computational model development. This assessment is supported with recent static high-pressure ultrasonic and x-ray diffraction data [Amulele *et al.*, 2008]. Newly available strength scaling studies [Kirkland *et al.*, 2009; Wereszczak *et al.*, 2009] are also integrated into the study. Results for both critical ceramics represent the best assessment of partial efforts reported earlier.

A further effort in the present year's work continues the theoretical development of failure-induced damage and fragmentation of ceramics in the ballistic environment. Recent

experiments under the auspices of the U.S. Army Research Laboratory provide impetus for this study. These experimental investigations include the impact shatter of boron carbide composite plates by armor piercing projectiles [Moynihan *et al.*, 2002] and the edge-on impact of glass plates with high-speed photographic diagnostics [Straussberg *et al.*, 2008].

## Summary

The principle thrust of this effort continues to be the collection, assessment and presentation of shock wave and high-strain-rate data on ceramics and ceramic-like materials in support of the U.S. Army TARDEC/ARL program on vehicle armor development. The emphasis focuses on characterization of dynamic material response within the armor impact and penetration environment for purposes of computational and engineering model development and assessment. Progress towards this end is summarized here and described in detail within the remainder of the report.

Specifically, the following accomplishments are documented in the present report:

- Shock wave Hugoniot data for tungsten carbide ceramic from various earlier sources are here assessed and synthesized. These shock Hugoniot data yield a hydrodynamic EOS for tungsten carbide that can be used as the basis EOS for a computational constitutive model. Further, shock wave measurements on tungsten carbide ceramics are used to assess dynamic compressive strength and spall strength. Additionally, a first-order relation is provided that determines the dependence of these strength properties on the metal content of tungsten carbide ceramic.
- EOS compression determined from the large anvil ultrasonic data is remarkable good but is affected by the porosity of the ceramic. Consistencies of the data through the arguments provided, however, lend added support for an earlier hydrodynamic EOS assessed from shock wave data. The ultrasonic compression curve for monolithic WC does demonstrate the substantial compression necessary to eliminate small amounts of porosity. This complication must be taken under consideration when modeling equation of state and strength properties of ceramics where porosity is a frequent constituent of the material.
- Although large anvil ultrasonic data for WC appear unduly effected by microstructure porosity, the corresponding data for WC-6%Co provides promising results for purposes of establishing and verifying the hydro equation of state of tungsten carbide. The ultrasonic data extrapolated to high pressure through both finite strain theory and a linear shock velocity particle velocity functional relation are compared with mixture theory predictions of compressibility. The ultrasonic data and analysis sensibly constrain the WC hydro equation of state.
- A comparative assessment of recent diamond anvil cell x-ray diffraction compressibility and shock Hugoniot compressibility of tungsten carbide is undertaken. A physics-based appraisal of the diamond anvil test on hard materials



suggests that nonhydrostatic stress levels brought about by crystal grain flocculation in the case of WC and component differential compressibility in the case of WC-6%Co are achieved that are comparable to those experienced in shock compression. Analytic modeling of the experimental offset predicts a nonhydrostatic strength offset comparable to compression under shock wave loading. Consequently, overlay of x-ray diffraction compression and the shock Hugoniot observed in experiment over much of the higher-pressure range is physically sensible.

- A systematic assessment of earlier analysis of shock wave and high-pressure-ultrasonic data for boron carbide is undertaken. Detailed analysis and shock physics arguments determine the occurrence of two polymorphic phase transformations within the range of the high-pressure data. Transformation pressures and transformation volumes are determined for the phase transitions. Further, hydrodynamic equation-of-state parameters are determined through the full range of the data appropriate for application in computational modeling.
- Experimental measurements of the size scale dependence of strength of boron carbide ceramic have recently become available. Experimental shock wave measurements of the dynamic strength of boron carbide are compared with the static strength scaling data and shown to be in remarkably good agreement. Size scale in the shock wave test is established by the shock wave risetime through which ceramic strength is exceeded and failure occurs. This consistency of dynamic (shock) and static strength has implications of time-dependent strength and strength modeling in this ceramic and probably other highly brittle solids.
- Theoretical modeling of statistical fragmentation in the ballistic environment initiated in the previous year's reports has been broadened. Following impetus provided by agreement to give an invited presentation at the American Ceramic Society annual meeting on the topic, an exposition contrasting dynamic fragmentation in ductile and brittle solids is given in the present report. A key emphasis in this description relates to the marked differences in fragment size distributions resulting from ballistic events in both ductile and brittle solids. Fragment size distributions for ductile materials are exponential or near-exponential in functional form and constrained by a single size scale. In contrast, fragmentation in brittle solids results in power-law distributions and two physical size scales that bound the fragment size distribution. Governing length scales in the fragmentation process are calculated through the theory from physical properties of the materials, and energetics of the impact event.
- Recent experimental work performed through auspices the Army Research Laboratory provides key test data for the fragmentation modeling development and verification. These data include fragmentation of boron carbide composite plates subjected to armor piercing projectile impact and high-speed photographic observation of fragmentation due to edge-on impact of glass plates. The former provides clear evidence of power-law distribution fragmentation of the boron carbide ceramic. For the latter plate-impact experiments, the theory reveals the time-

dependent nature of the fragmentation wave front clearly observed in the photographic records.

## II Background

The benefits of using computers to simulate the interactions of weapons and armor systems are readily apparent. Economics and system/materials optimization are among the obvious benefits. There are challenges, however, that must be overcome before such computational tools become fully reliable and can realize the many available benefits. Namely, the description of materials and their response within the extreme terminal ballistic environment must be faithful.

Similarly, imaginative engineering models based on good physical understanding of the ballistic phenomena have, and will continue to have, an important role in the assessment of armor and weapon performance.

In both computational and engineering endeavors, the dynamic material response and the constitutive models describing material response over the range of deformations and thermodynamic conditions experienced must be fully understood and adequately characterized.

Within the present effort, these issues are restricted to ceramics and ceramic-like materials including glass and glass ceramics, and their role as armor components within the armor/anti-armor terminal ballistic event. The physics of failure and deformation of brittle solids such as ceramics and glass within the terminal ballistic environment is not yet fully understood. Phenomenological behaviors such as dwell, failure waves, fracture kinetics, fragmentation and phase transformation are still topics of active research. Consequently, computational constitutive models developed to describe the response of ceramic materials in armor applications must be viewed as work in progress. Nevertheless, advancements are continuing to be made on model development, and improvements can be expected to continue.

Engineering ceramics are commonly complex polycrystalline solids in which detailed chemical and material processing methodologies have been developed and pursued to enhance specific properties critical to the intended system performance. This careful tailoring of ceramic properties to improve performance is rapidly maturing in the armor application of ceramics. Microstructure features such as porosity, second phase materials, and controlled anisotropy, among others, are increasingly being recognized as either detrimental to, or an enhancement to, armor performance under specific conditions.

Even transparent glass, which emerges as an important armor material of interest, when examined on an adequately small length scales, exhibits a stress concentrating defect structure which must play a role in the strength and ultimate failure of glass and glass bearing structures.

One difficulty arises in determining constitutive models that adequately describe the dynamic response of the new materials in computer simulations of ballistic events. The cost in time and resources, which would be necessary to perform the usual suites of material properties

tests on new materials of interest, becomes rapidly exorbitant. It therefore becomes necessary to pursue other, more expedient, methods to estimate sensible response models.

It is possible, in certain cases, to adequately estimate equation of state and dynamic strength properties of more complex engineering materials through appropriate mixing or extrapolation/interpolation of the properties of this material's simpler component materials. For example, it is possible to make reasonable estimates of the equation of state and strength of a porous ceramic if the corresponding properties of the monolithic ceramic are available. Or, as another example, when appropriate properties of component materials are known, sensible descriptions of the constitutive equation of state of a ceramic mixture of these components can be determined.

Further, experimental studies by other test techniques, when the complementing physics is understood can contribute markedly to material model development and validation. The present report uses experimental data on ceramics from high-pressure ultrasonic measurements, diamond anvil cell x-ray diffraction data and strength scaling studies through indentation hardness.

Within the charter of the present program of surveying and analyzing earlier shock wave and high-rate data for armor ceramics, analysis and theoretical modeling is continued with emphasis on extracting information from these earlier data that are relevant to the physical understanding and modeling of the ballistic event. Both recently developed, and earlier, but not commonly known, analysis and theoretical approaches are pursued. Applications of the theoretical efforts and analysis are examined in light of available data for ceramics and glass.

### III Tungsten Carbide Ceramic EOS and Strength

The dynamic equation of state (EOS) and strength properties of tungsten carbide ceramic have been developed almost exclusively from shock compression data. Recently, high-pressure static compression data have been provided by Amulele *et al.* [2008]. Their work includes both diamond anvil synchrotron x-ray diffraction data as well as large-volume high-pressure ultrasonic measurements. X-ray diffraction measurements are up to 50 GPa while ultrasonic measurements are to 14 GPa. Further, measurements are provided for both a monolithic tungsten carbide and a tungsten carbide 6% cobalt mixture. Disturbingly, marked differences are observed between the x-ray diffraction compressibility and extrapolation of the ultrasonic measurements.

Past shock wave data on tungsten carbide ceramic have not previously been collectively examined. This effort is undertaken here and critical comparisons are made with the recent static compression data. The shock equation-of-state data were obtained on both a monolithic (nearly pure) tungsten carbide as well as several liquid phase sintered ceramics with nominal metal content. Features of the shock EOS are examined first. Comparisons are then made with the static high-pressure EOS data. Lastly, compression dynamic strength and spall strength established from shock wave profile measurements complete the constitutive EOS and strength properties investigation of tungsten carbide.

#### *Tungsten Carbide Ceramic and Composition Effects*

Tungsten carbide ceramics are commonly produced with metal additives through liquid phase sintering methods. Metal additives are typically in the range of 5% to 10% by weight. Commonly, cobalt is the dominant component of the metal additive. Such composition complications are expected to influence both the dynamic equation of state and the strength properties of the tungsten carbide ceramic.

Tungsten carbide crystallizes in a hexagonal structure. Crystal strength is high and hot-pressed monolithic ceramics prepared from the WC powder exhibit comparable strength. Strength in the shock-compressed state is still under exploration, although initial investigation indicates substantial retained strength [Dandekar and Grady, 2002]. The addition of metal reduces ceramic compressive strength, but increases the toughness improving both fracture resistance and dynamic spall strength.

Recently, Amulele *et al.* [2008] have performed synchrotron x-ray diffraction measurements on polycrystalline powder samples loaded in a diamond anvil cell, as well as ultrasonic measurements on hot-pressed ceramics compressed in a multianvil high-pressure apparatus, and determined the pressure versus volume relations for WC and WC-6wt%Co up to 50 GPa. These new data when combined with previous shock wave Hugoniot measurements on comparable WC ceramics offer additional perspective in refinement of the dynamic equation-of-state and strength properties for this material.

In the present section shock wave Hugoniot data and the recent static high pressure data are used to investigate the effects of composition variations (porosity and metal additives) on the shock equation of state and strength of tungsten carbide ceramic. The study joins earlier microstructure models of large amplitude mixture compressibility [Grady, 2003] with the experimental data to assess the desired equation of state and strength properties.

## Tungsten Carbide Materials

Shock wave equation-of-state properties are investigated for several tungsten carbide ceramics. The shock Hugoniot data of McQueen *et al.* [1970] are included. The material tested in their study was a near-full-density tungsten carbide ceramic with 5wt% Co. Shock data for two other pressureless liquid phase sintered tungsten carbide ceramics are also included in this comparison. One is produced by Kennametal Company, and contains 5.7wt% Co, 1.9wt% Ta, along with less than 0.3wt% Nb and Ti. Several Hugoniot points along with shock strength properties were measured for this material. The second tungsten carbide material was extracted from armor piercing (AP) rounds. This tungsten carbide ceramic contained 3-4wt% Ni, 0.4-0.8wt% Fe and 0.05-0.2wt% Co. Only shock strength properties were determined for this latter material. Selected data analyses on the latter two materials have been previously reported [Grady, 1995, 1999]. Finally, Hugoniot and strength data are provided for a hot-pressed high-purity tungsten carbide produced by Cercom Company. The same material was investigated in the study of Amulele *et al.* [2008]. The material is reported to be 97.2wt% WC and 2.8wt% W<sub>2</sub>C, the latter resulting from the densification process. Theoretical densities from WC and W<sub>2</sub>C are 15700 kg/m<sup>3</sup> and 17200 kg/m<sup>3</sup>, respectively. The material is also reported to have about 1% porosity. Later information noted that this WC was not fully binder free. The material contained about 2 wt% Co and less than 1wt% each of Ni and V. The grain size was about 0.5-1.5  $\mu\text{m}$ . Shock strength and equation-of-state analyses of the shock wave data on this ceramic have previously been presented by Dandekar and Grady [2002]. Density and elastic properties for the selected tungsten carbide ceramics are provided in Table (1).

Table 1. Density and Elastic Properties of Tungsten Carbide Ceramic

Material	Density (kg/m <sup>3</sup> )	$c_l$ (km/s)	$c_s$ (km/s)	$c_o$ (km/s)	Bulk Modulus (GPa)
LANL <sup>1</sup>	15010	6.89	4.18	4.92	363.0
KM <sup>2</sup>	14930	6.90	4.17	4.94	364.5
AP <sup>3</sup>	14910	6.92	4.15	4.99	371.4
Cercom <sup>4</sup>	15560	7.04	4.30	4.96	383.0
<sup>1</sup> Tungsten Carbide (5wt% Co), Los Alamos National Laboratory, McQueen <i>et al.</i> [1970].					
<sup>2</sup> Refers to K68 material obtained from Kennametal Company.					
<sup>3</sup> Material extracted from 14.5 mm (BS-41) armor piercing round.					
<sup>4</sup> High purity tungsten carbide ceramic from Cercom Company.					

## Hugoniot Properties of Tungsten Carbide Ceramics

Plots of experimental Hugoniot data for tungsten carbide ceramics are shown in Figure (1). Shock velocity versus particle velocity states are provided on the left while the Hugoniot pressure versus particle velocity representation is shown on the right. As is readily observed, neither shock velocity nor shock impedance is markedly affected by the variations in composition among the three ceramics. The high-purity Cercom ceramic is observed to be modestly stiffer in both plots, followed, respectively, by the Kennametal material and the ceramic tested by McQueen *et al.* [1970]. Elastic wave speeds are compared with the shock velocity data on the left. Hugoniot elastic limit (HEL) amplitudes for the Cercom ceramic ( $\sim 6$  GPa) and the Kennametal ceramic ( $\sim 4$  GPa) are identified on the right. Curves in either plot represent a sensible average of all of the experimental Hugoniot data.

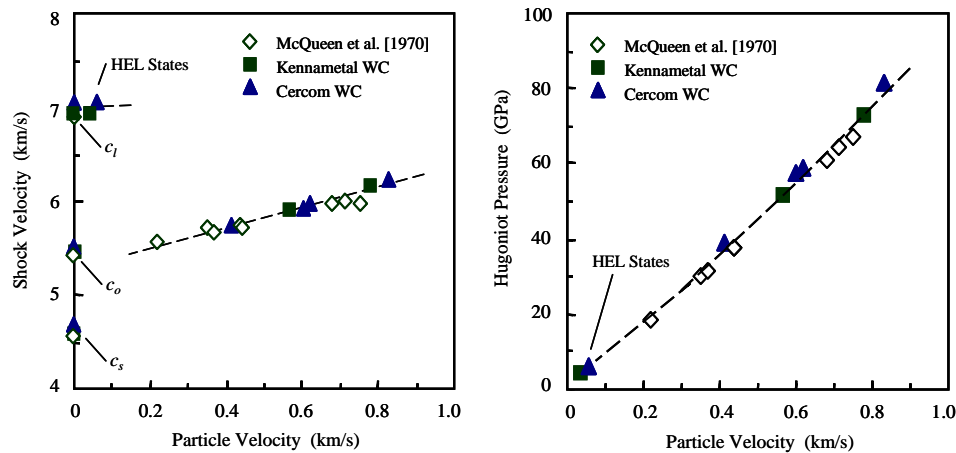


Figure 1: Experimental shock velocity versus particle velocity and pressure versus particle velocity Hugoniot data for tungsten carbide ceramics.

A further display of the same Hugoniot data is provided in Figure (2) in both a Hugoniot pressure versus specific volume and a Hugoniot pressure versus compression representation. Again, the Hugoniot compression representation reveals modest but increasing steepness of the Hugoniot curves for the McQueen *et al.*, Kennametal, and Cercom materials, respectively.

## Hydrodynamic Response

Through selective use of the very high pressure Hugoniot data of McQueen *et al.* [1970], a sensible hydrodynamic compression curve for monolithic tungsten carbide has been constructed [Dandekar and Grady, 2002]. A compression relation of the linear shock velocity versus particle velocity form,

$$p = \frac{\rho_o C_o^2 (1 - \rho_o v)}{(1 - S \rho_o v)^2}, \quad (1)$$

with  $\rho_o = 15700 \text{ kg/m}^3$ ,  $C_o = 4.93 \text{ km/s}$  and  $S = 1.31$  was determined from analysis of the shock data. It is important to recognize that such an effort is subject to uncertainties due to unknown initial sample porosities and additives, along with possible subtle phase changes on the Hugoniot not recognized in the experimental data. Uncertainties due to these unknowns are difficult to bound. When joined with the recent large-anvil ultrasonic data of Amulele *et al.* (2008) that is analyzed for dynamic equation-of-state purposes in subsequent sections, reasonable EOS uncertainty is ascribed through comparative assessment of the two starkly different test methods. The two test methods lead to a nominal  $\pm 1.5\%$  in volumetric strain at pressure, with the EOS of Dandekar and Grady residing towards the more compliant bound of this uncertainty.

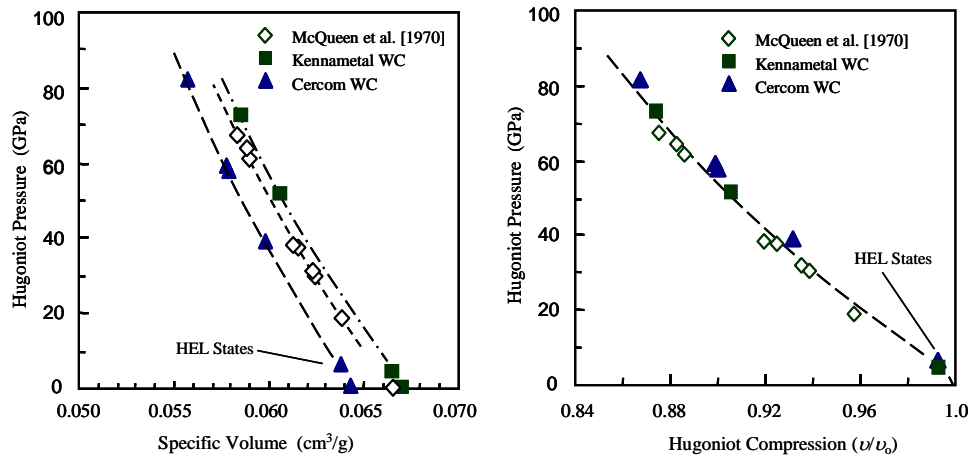


Figure 2: Experimental pressure versus specific volume and pressure versus compression Hugoniot data for tungsten carbide ceramics.

A description of the shock equation of state response of any of the tungsten carbide ceramics can be generated through the monolithic hydrodynamic response of Equation (1) and the methods for modeling the compositional mixtures described in an earlier report [Grady, 2003]. The Cercom ceramic, accounting for the small admixture of  $\text{W}_2\text{C}$ , has a theoretical density of  $\rho_o = 15740 \text{ kg/m}^3$ . The measured density of  $\rho_{oo} = 15560 \text{ kg/m}^3$  yields a calculated porosity of 1.1% – in good agreement with the independently reported porosity of about 1% [Dandekar and Grady, 2002].

Compression curves for both the partial-volume averaged iso-pressure, and the partial-pressure averaged iso-compression equation-of-state response are shown with the Hugoniot data for the Cercom ceramic in Figure (3). The difference between the two curves is a consequence of the initial porosity. Equation-of-state compression is predicted to transition from the iso-compression to the iso-pressure curve as compaction of the porosity takes place under shock compression. The compaction process probably requires several tens of GPa to achieve completion. Shock compaction experiments on tungsten carbide powder reveal that the material retains approximately 8% porosity following shock compression to stresses in



excess of 4 GPa [Vogler *et al.*, 2007]. This experimental observation may have relevance in the interpretation of diamond anvil cell x-ray diffraction measurements on compressed tungsten carbide powders.

Similar iso-pressure and iso-compression equation-of-state curves are shown for the McQueen *et al.* [1970] material assuming the reported composition of WC-5wt%Co. Calculated and measured densities provide a 0.7% discrepancy. The discrepancy is assumed here to be due to initial porosity. Again, the principal difference between the two curves is due to the assumed porosity. A comparable calculation also accounting for the differing compressibilities of cobalt and tungsten carbide do not markedly affect predicted compression curves.

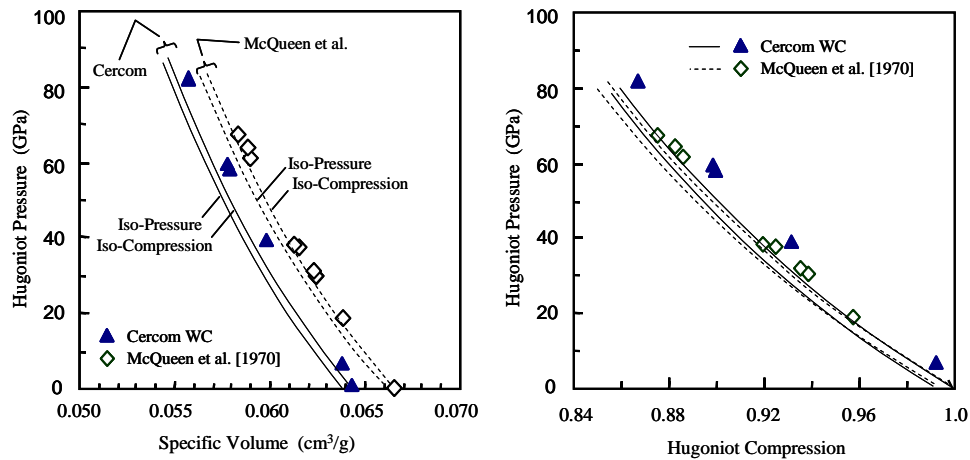


Figure 3: Hugoniot compression of tungsten carbide ceramics and model predictions of the hydrodynamic equation-of-state compression accounting for compositional differences.

For both materials, the Hugoniot data resides above the model representation of the equation-of-state hydrodynamic compression. Accepting the relation developed for the hydrodynamic response of the monolithic tungsten carbide, and appropriate application of the compositional model, the discrepancy is attributed to strength (deviator stress) on the Hugoniot. The same conclusion was reached previously for the Cercom ceramic [Dandekar and Grady, 2002]. The strength offset for the Cercom material is of order 10 GPa. The offset for the McQueen material is somewhat less. The offset of the Cercom material is sensibly consistent with measured initial HEL amplitude and post-HEL hardening behavior determined from shock profile experiments [Dandekar and Grady, 2002].

## Static High-Pressure and Shock Hugoniot Compression EOS

Static isothermal and isentropic compression EOS properties of WC and WC-6%Co have been experimentally assessed through synchrotron x-ray diffraction measurements on diamond anvil compression of powder samples, and through ultrasonic measurements on ceramic samples in a large-volume multi-anvil high-pressure apparatus. The details of this extensive study are provided by Amulele *et al.* [2008].

The x-ray diffraction measurements and ultrasonic EOS curves for both WC and WC-6%Co from Amulele *et al.* [2008] are shown on the left in Figure (4). These ultrasonic curves represent extrapolation of ultrasonic measurements up to 14 GPa based on a best fit to a third-order Birch-Murnaghan equation of state.

The additional solid curve on the left is that of a hydrodynamic equation of state based on a best assessment of shock Hugoniot data [Dandekar and Grady, 1992]. This curve is a best-assessment linear shock velocity versus particle velocity representation of this shock hydrodynamic EOS with  $\rho_o = 15700 \text{ kg/m}^3$ ,  $C_o = 4.93 \text{ km/s}$  and  $S = 1.31$  as noted previously. Based on  $K_o = \rho_o C_o^2$  and  $K'_o = 4S - 1$  the bulk modulus and pressure derivative for this EOS curve is  $K_o = 381.6 \text{ GPa}$  and  $K'_o = 4.24$ .

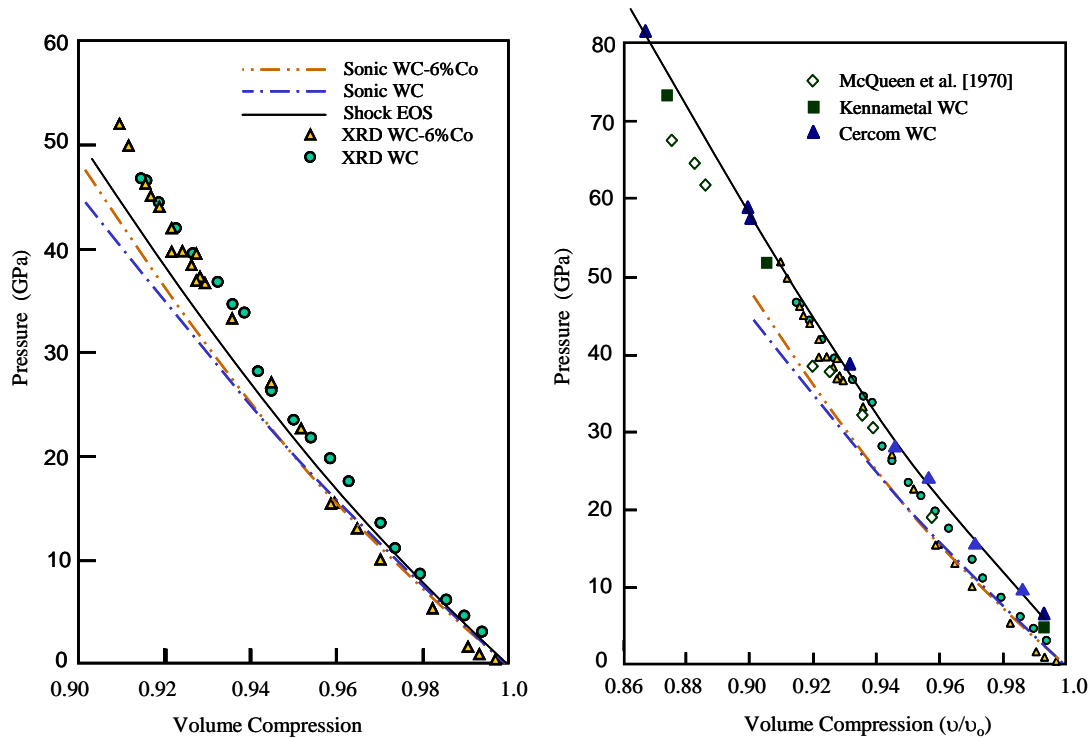


Figure 4: The ultrasonic and x-ray diffraction measurements from Amulele *et al.* [2008] for both WC and WC-6%Co are displayed on the left. The one additional solid curve is a hydrodynamic equation of state for monolithic WC assessed from shock wave Hugoniot data by Dandekar and Grady [2002]. The static data are compared with shock Hugoniot data on the right.

The same ultrasonic and x-ray diffraction data are compared with the shock Hugoniot data on the right in Figure (4). The monolithic WC (Cercom material) for which shock Hugoniot data is provided is the same material studied in the static high-pressure ultrasonic studies.

The outwardly apparent disparity between the ultrasonic and x-ray-diffraction-determined compression equations of state, and their comparisons with the shock Hugoniot data, are worthy of closer examination before any attempt is made to use these data for computational constitutive model development.

## Ultrasonic EOS

One difficulty concerns use of the monolithic WC in the ultrasonic measurements. This material, as discerned from both direct observation, and assessment of the bulk density with the theoretical densities of WC and  $W_2C$  (this material includes a small amount  $\sim 2.8\%$  of this latter compound), contains a void volume, or porosity, of about 1%. The microscopic character of this porosity is important, but is not known. One manifestation of this porosity is reflected in the discrepancy between the ultrasonic longitudinal and shear wave speeds and the extrapolation to zero pressure of the high-pressure ultrasonic measurements Amulele *et al.*, [2008]. Note that a similar discrepancy is not observed for the liquid phase sintered WC-6%Co where negligible porosity is expected in this material. The porosity in the WC ceramic is apparently not irreversibly removed when compressed to 14 GPa, as the authors report full recovery of original dimensions on unloading to zero pressure.

Reversible compression of the pore space during pressure loading can soften the compressibility of the bulk material and potentially detract from the assessment of the crystal lattice compressibility of the WC. This effect may be reflected in the somewhat low value of  $K'_o = 2.61$  reported for the WC from the ultrasonic measurements.

The shock EOS assessed from Hugoniot data for WC, also shown on the left in Figure (4), and the ultrasonic EOS have essentially the same initial compressibility (very similar  $K'_o$ ). The former shock EOS, however, reports a markedly higher  $K'_o = 4.24$ , leading to the noticeably stiffer response at high pressure. This measure of nonlinearity of the lattice compressibility is assessed from the higher-pressure shock Hugoniot data, and can be subject to its own experimental uncertainties. Foremost among these is variations of strength with increasing pressure on the Hugoniot. Commonly, strength decreases because of increased heating with pressure on the Hugoniot. If this were the case, a  $K'_o = 4.24$  should be a lower bound for the lattice compressibility nonlinearity as assessed from Hugoniot data.

A further concern is that the ultrasonic WC-6%Co curve is stiffer (less compressible) at high pressures than is that of the monolithic WC ceramic curve. Cobalt is actually more compressible than tungsten carbide and thus the WC-6%Co should be more compressible than the monolithic WC. Comparison of the ultrasonic EOS curve for WC-6%Co and the shock hydrodynamic EOS for WC on the left in Figure (4) is qualitatively correct in this regard

The large anvil ultrasonic data for the WC-6%Co is also influenced by microstructure. Porosity is not an issue, however. Compressibility of the component cobalt and tungsten carbide is shown on the left in Figure (5). Compressibility for cobalt follows from the Los Alamos database [Marsh, 1980]. The hydrodynamic compressibility of Dandekar and Grady [2002] is assumed for WC.

Bounding estimates of the ultrasonic properties of a mixture of tungsten carbide and 6% cobalt (approximately 10% by volume) are readily determined [*e.g.*, Grady, 2003], and shown with the same single component curves in the figure.

On the right in Figure (5) extrapolations based on the large anvil ultrasonic measurements of Amulele *et al.*, [2008] are compared with the WC-6%Co mixture upper and lower bound compressibilities, and the hydrodynamic equation of state for WC of Dandekar and Grady [2002] based on shock Hugoniot data. Finite strain extrapolations for both WC and WC-6%Co of Amulele *et al.*, [2008] are identified by (A) in the figure. A further curve is a linear shock velocity versus particle velocity extrapolation of the same ultrasonic data for WC-6%Co.

The conclusion from this comparison is that the two extrapolations of the large anvil ultrasonic data for WC-6%Co fall outside of (above) the upper-lower bound mixture prediction, but not by much. Since the mixture prediction is based on the hydrodynamic compressibility of WC determined by Dandekar and Grady [2002], the experimental comparison supports this curve, or perhaps a slightly stiffer curve, dependent on the degree of accuracy ascribed to the data and the extrapolation. The two test methods lead to a nominal  $\pm 1.5\%$  in volumetric strain at pressure, with the EOS of Dandekar and Grady residing towards the more compliant bound of this uncertainty.

Again, the ultrasonic extrapolation compression curve for WC of Amulele *et al.*, [2008] is inconsistent with the other data evaluated here, and probably unduly influenced by initial microscopic porosity in the test material. In particular, the extrapolated EOS curve for WC is more compliant than that for WC-6%Co – a result that is physically unreasonable.

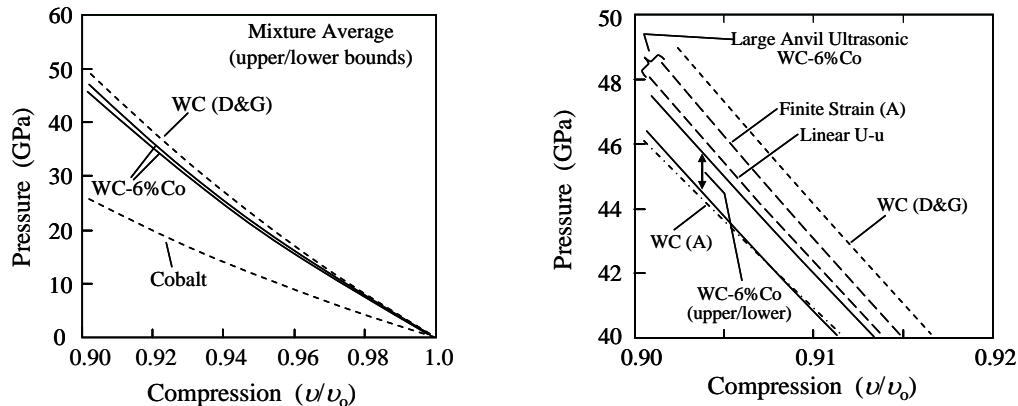


Figure 5: Compressibility of cobalt [Marsh, 1980] and tungsten carbide [Dandekar and Grady, 2002] or (D&G) and upper and lower bound mixture compressibility of WC-6%Co is shown on the left. Comparisons on the right are made with extrapolations of large anvil ultrasonic data of Amulele *et al.* [2008] or (A).

## X-Ray Diffraction Compressibility

In contrast to extrapolation of the large anvil ultrasonic data, the compressibility of tungsten carbide through x-ray interrogation exhibits markedly stiffer response in the experimental data of Amulele *et al.* (2008). This behavior applied to both crystalline WC as well as the tungsten carbide and cobalt mixture WC6%Co. In fact, in the higher pressure 30-50 GPa

range the x-ray diffraction pressure versus compression states fall remarkably close to the tungsten carbide shock Hugoniot.

The relative differences in compressibilities inferred from ultrasonic, diamond anvil x-ray diffraction, and shock Hugoniot raise questions concerning the equation-of-state implications of the various data sets. A number of factors can contribute to the observed discrepancy, including material microstructure, chemistry, and sample size scale. Uncertainties in test methods can also play a role. The focus here, and believed to be a first order influence, is that of nonhydrostatic stress states in the DAC x-ray sample due to multi-crystal interaction during the compression process. In the following discussion, some of the physics and mechanics issues associated with the diamond anvil cell (DAC) measurements on hard materials such as tungsten carbide are explored. The tentative conclusion is that the DAC x-ray diffraction compression measurements exhibit material strength comparable to the shock Hugoniot data. The experimental techniques described by Amulele *et al.* (2008) are considered to provide quantitative assessment of the measurement.

A preindented plate (commonly stainless steel) is center drilled to provide a cylindrical cavity approximately 35  $\mu\text{m}$  in depth and 130  $\mu\text{m}$  in diameter. Sodium chloride (NaCl), among others, is inserted into this cavity as a pressure transmitting medium. 1-2  $\mu\text{m}$  grain size WC powder is then introduced into the same cavity in sufficient quantity to provide adequate x-ray signal strength. Gold grains, among other possible materials, are further introduced to provide the internal pressure calibrant.

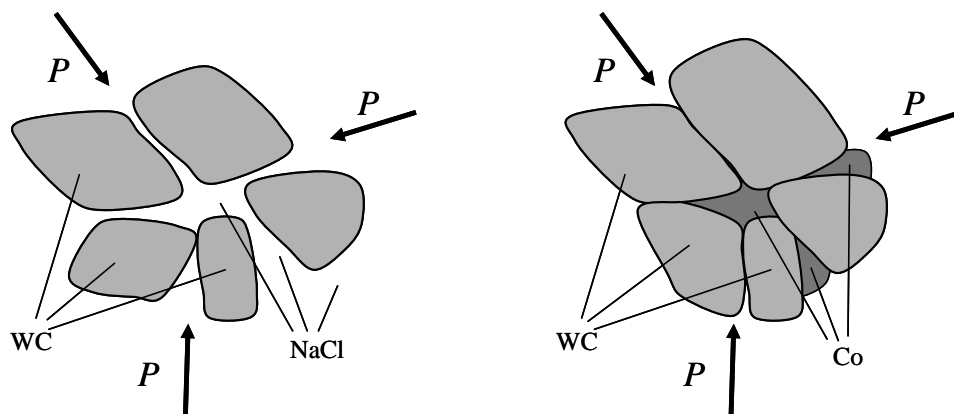


Figure 6: Loosely bound agglomerates of tungsten carbide grains are illustrated on the left. On the right a granular assembly of tungsten carbide with cobalt interstices is depicted.

Independent grains of WC pressurized within the NaCl medium would exhibit near hydrostatic compression and appropriate equation-of-state compressibility. Difficulties arise because powders flocculate and complicate the pressure transmission process. Several examples are illustrated schematically in Figure (6). On the left some number of grains of WC are loosely joined as the pressurization initiates. On the right grains of WC with interstices of cobalt are depicted. Efforts, of course, should be made to minimize multi-crystal interactions in striving for full hydrostatic compression. This objective is clearly difficult, however, because of the extremely small active volume region in the DAC test.

The large compressibility of NaCl relative to that of WC requires the flow of NaCl and intrusion of additional NaCl through the narrow constrictions between grains would be required to maintain hydrostatic pressure on the WC grains. If flow is restricted then regions within the WC granular agglomerate will become under pressured and compression of the grains will be nonhydrostatic. Similarly, on the right, compressibility of cobalt is higher than that of WC and comparable nonhydrostatic stress conditions will emerge as the transmitting pressure is increased. The relative compressibilities of WC, Co and NaCl are illustrated in the left in Figure (7).

A perhaps overly simplified model leading to comparable nonhydrostatic stresses is illustrated in Figure (7), where an agglomerate of WC grains is represented by a spherical shell of WC with a spherical central cavity representing void, NaCl or Co, each exhibiting higher compressibility than WC. Further, flow of pressure transmitting medium into this cavity is assumed prohibited. Increasing pressure  $P$  leads to elastic radial and circumferential stresses  $\sigma_r$  and  $\sigma_\theta$  in the WC shell that are dependent on the radial position  $r$  with  $a \leq r \leq b$ . Failure through a critical stress difference  $\sigma_r - \sigma_\theta = Y$  first occurs at the inner radius  $r = a$ . Here,  $Y$  is assumed a constant yield stress although similar logic would apply to other failure mechanisms such as brittle fracture. As the pressure  $P$  is increased, yield ultimately subsumes the entire shell of WC.

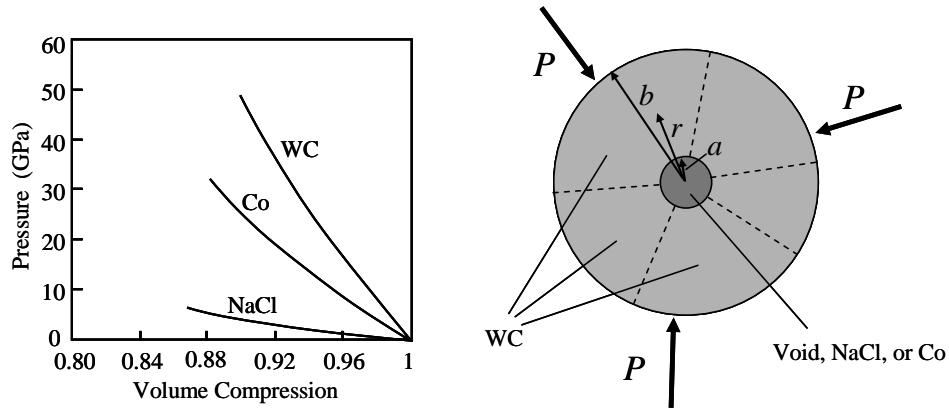


Figure 7: Relative compressibility is shown for tungsten carbide, cobalt and sodium chloride. Nonhydrostatic pressurization of an agglomerate of tungsten carbide grains is modeled as a spherical system.

Material throughout the shell then support a mean stress  $\bar{\sigma}$  and a deviator stress at the failure limit that is characterized by the failure property  $Y$ . Thus, the measured pressure  $P$  in the pressure-transmitting medium relates to the stress in the WC in the neighborhood of the WC-NaCl boundary according to,

$$P = \bar{\sigma} + \frac{2}{3}Y. \quad (2)$$

The mean pressure  $\bar{\sigma}$  will establish the lattice compression and the volume strain determined by the x-ray diffraction measurement. The shear stress difference  $\sigma_r - \sigma_\theta = Y$  will contribute modest distortion to the lattice.

Equation (2) is the same expression that relates the Hugoniot pressure to the mean pressure and the stress offset in materials that exhibit strength on the Hugoniot. Consequently, the near overlay of the x-ray diffraction compression data and the shock Hugoniot for tungsten carbide is physically sensible. Further, whether WC powder or WC6%Co is subjected to DAC x-ray diffraction testing would not markedly alter this conclusion as is observed in the test data comparison in Figure (4).

Based on best syntheses of the large-anvil ultrasonic, diamond anvil x-ray diffraction, and available shock Hugoniot data Hugoniot and dynamic hydrostatic compression curves for WC and WC-6%Co are shown in Figure 8.

The dynamic hydrostat for WC is based here on the EOS provided by Dandekar and Grady (2002) although the ultrasonic data of Amulele *et al.* (2008) could be used to argue a slightly stiffer curve. The correction, however, would be modest. The dynamic hydrostatic EOS for WC-6%Co is based on a mixture average of tungsten carbide and cobalt as described earlier. The Hugoniot data shown are respectively that for Cercom WC [Dandekar and Grady, 2002] and for WC-6%Co McQueen *et al.* [1970].

## Dynamic Strength and Composition

Shock wave strength features are influenced by compositional variations in tungsten carbide ceramic. Both the dynamic compressive strength (HEL) and dynamic tensile strength (spall stress) have been measured for several of the tungsten carbide ceramics reported on here. Spall stress as a function of the shock wave pre-compression stress is plotted on the left in Figure (9). Both spall stress and Hugoniot elastic limit are plotted on the right as a function of the metal content of the ceramic. Metal content clearly increases the dynamic tensile strength and decreases the compressive shock strength as observed in contrasting the two liquid-phase sintered ceramics with the hot-pressed Cercom tungsten carbide. Further, strength dependence on specific metal content and preparation method is suggested by the marked difference in spall strength between the two liquid-phase sintered materials. Also significant is that spall stress measurements on the metal phase tungsten carbide ceramics in the left-hand plot achieve shock pre-compression stress levels in excess of the HEL of the material, suggesting little or no fracture damage during compressive yield. In contrast, reduction of

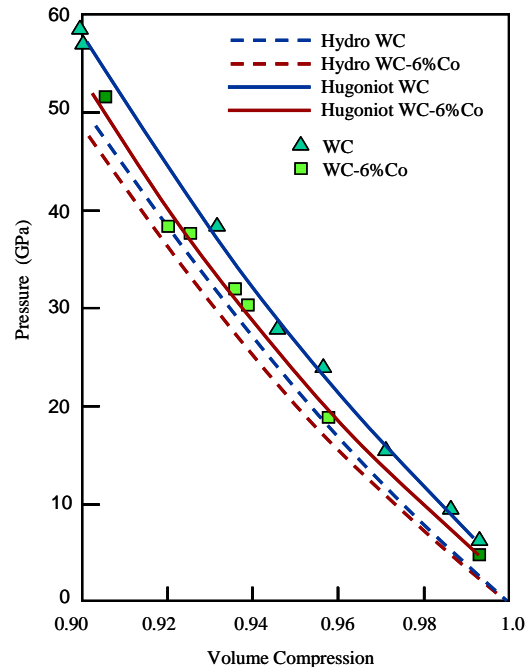


Figure 8: Hugoniot and dynamic hydrostatic compression for WC and WC-6%Co.

spall strength of the Cercom material as pre-compression stress approaches the HEL may reflect some weakening of the ceramic due to compressive fracture damage. This same trend has been noted in the spall strength of selected silicon carbide ceramics [Dandekar and Bartkowski, 2001].

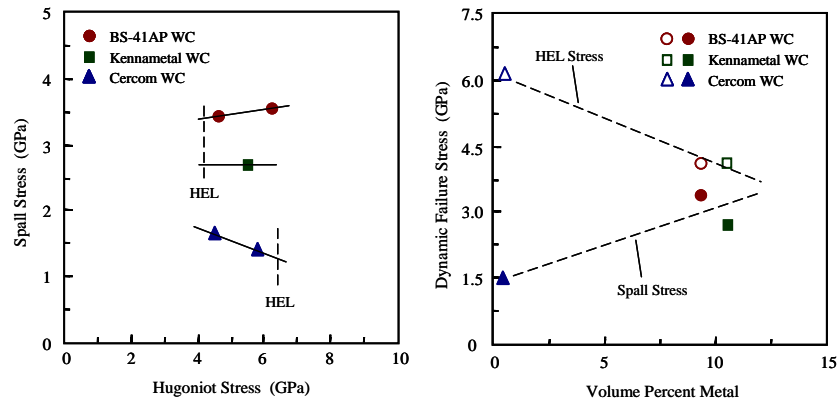


Figure 9: Tensile spall strengths and compressive Hugoniot elastic limit (HEL) strengths for tungsten carbide ceramics showing dependence on shock pre-compression stress and ceramic metal content.



## IV Boron Carbide Ceramic EOS and Strength

Boron carbide ceramic has promising potential for armor application. There is a pressing need for a confident strength and equation-of-state (EOS) model for computational simulations of ballistic performance in a range of armor functions. Consequently, boron carbide has been tested extensively in recent years in terms of both ballistic performance and its dynamic material response. Testing has revealed atypical dynamic strength and EOS properties. In spite of considerable effort, development of an adequate computational model for boron carbide has proven problematic and an appropriate model is not yet available.

Shock wave and static-high-pressure data have previously been addressed in the present program [Grady, 2001; 2002] for purposes of supporting computational model development. A systematic assessment of these earlier efforts, however, has not yet been undertaken. This assessment has now been carried out and is the principal topic of the present section.

As noted, boron carbide ceramics have been particularly problematic in attempts to develop adequate constitutive model descriptions for purposes of computational simulation of dynamic response. Dynamic strength properties of boron carbide ceramic differ uniquely from comparable ceramics, and are difficult to characterize. Further, boron carbide is believed to undergo polymorphic phase transformation within the shock wave compression process. These phase transformation features have been particularly elusive under experimental investigation, and consequently are also difficult to capture within an appropriate constitutive model.

It should also be noted that the early test of McQueen *et al.* [1970] on slightly distended (porous) boron carbide suggests a technique for improved assessment of the dynamic hydro-compression through elevated temperature states and the concomitant reduction of nonhydrodynamic stress states. Further shock testing pursuing this approach in further detail should be considered.

Also as noted above, boron carbide ceramic is an attractive candidate for ballistic applications. It is the lowest density and the highest strength ceramic among a suite of ceramics under consideration for such applications. The necessary physical and mechanical properties of boron carbide have been studied extensively and access into much of the literature is available in the report of Dandekar [2001]. In particular, the Hugoniot and ultrasonic data integral to the development of shock wave and high-strain-rate constitutive response models are reviewed in the same report. The present assessment is principally limited to high-pressure phase transformation in boron carbide ceramic and the hydrodynamic (non-strength) equation of state of the ceramic. Some issues concerning dynamic strength that were stimulated by more recent parallel studies [Kirkland *et al.*, 2009; Wereszczak *et al.*, 2009] are also addressed.

## *Phase Transformation from Shock Hugoniot Data*

Although other methods are being explored to characterize high-pressure phase transformation in ceramic materials, – diamond anvil cell technology for one – shock compression techniques remain the standard when issues of transition pressure and compressibility are of paramount concern. Extraction of the required phase transformation properties remains elusive, however, and usually requires concerted effort by workers experienced in the field. The extensive shock Hugoniot data for boron carbide provided by McQueen *et al.* [1970], in the LANL shock compendium [Marsh, 1980], are representative. These data, joined with the necessary analysis, provide strong evidence for phase transformation in boron carbide ceramic, in addition to the compressibility properties accompanying the phase transformation.

Boron carbide subject to high-rate shock wave compression exhibits dynamic strength, based on its Hugoniot elastic limit amplitude, that is one of the highest observed among the metal-nonmetal compounds. The strength of boron carbide ceramic subsequent to failure within the shock and post-shock domain is controversial, however, and considerable effort has been expended in achieving a better understanding of the underlying physics [Grady, 1994; Vogler *et al.*, 2004].

The restricted loading path of the shock wave experiment complicates interpretation of strength in the shock compression event. In particular, phase transformation under shock compression with accompanying change in specific volume and compressibility makes the assessment of strength on the Hugoniot particularly difficult. Phase transformation in boron carbide within the shock and high-rate loading environment has been suggested. Efforts have been undertaken to assess high-pressure phase transformation in boron carbide through static diamond anvil cell technology [Manghnani, 2007]. Recently Vogler *et al.* [2004] have identified evidence of phase transformation in boron carbide from shock wave experiments.

In this study, alternative analyses of shock wave data for signatures of phase transformation are pursued. The conclusion is that shock data alone strongly suggest the occurrence of one phase transformation in the shock compression process. Shock data combined with extrapolation of modest-pressure ultrasonic data suggests the occurrence of a second transition under shock compression. The arguments and supporting data for this interpretation follow. These efforts were previously detailed in unpublished reports [Grady and Doolittle, 2001; Grady, 2002]. The present effort brings these early efforts up to date with the inclusion of more recent high-pressure data.

The principle shock wave data for boron carbide ceramic applied in this analysis are that of McQueen *et al.*, [1970] provided in the Los Alamos Compendium [Marsh, 1980]. Other shock data on boron carbide are available [*e.g.*, Gust and Royce, 1971; Grady, 1994; Vogler *et al.*, 2004], but the former data have unique features significant to the present objectives. Further, additional uncertainties inherent in addressing the different materials and different experimental methods of the various authors are avoided.

Before proceeding, however, some qualifying remarks regarding the available Hugoniot data are of concern. There is a marked disparity between the high-pressure Hugoniot

compression data of Gust and Royce [1971] and of Vogler *et al.* [2004] on one hand, and the data of McQueen *et al.* [1970] and Grady [1994] on the other. Whether these differences are due to manifestations of material strength, effects of phase transformation, uncertainties in initial material composition and chemistry, or difficulties with analysis and interpretation of the measured shock data is not known. Some of the issues have been discussed by Dandekar [2001]. Additional comments concerning this disparity will be offered where relevant in the development that follows. This uncertainty in the available shock wave data for boron carbide remains puzzling, however, and a full explanation is not yet available.

The McQueen *et al.*, [1970] data provide shock compression states for boron carbide over the pressure range of approximately 15–110 GPa. These data encompass two starting densities for boron carbide of nominally 2400 kg/m<sup>3</sup> and 1900 kg/m<sup>3</sup>. Assuming reasonably pure material, the densities imply initial porosities of approximately 5% and 30%, respectively, based on a theoretical density of 2520 kg/m<sup>3</sup>. (Although ceramic composition was not reported, it is unlikely that any sintering additives would be lower density than the boron carbide. (Appreciable higher density additives, and correspondingly higher calculated porosity, could account in part for discrepancies with the Gust and Royce data, but this seems unlikely.) Shock velocity versus particle velocity ( $U - u$ ) and pressure versus specific volume ( $p - v$ ) Hugoniot data for the boron carbide are shown in Figure (10). In the test method of McQueen *et al.* [1970] shock velocity and particle velocity are the measured quantities and are identified as the original data in the right hand plot. There are two regimes and two curves associated with the two sets of different initial porosity data. The scatter for the most part is due to sample-to-sample variations in initial density. Pressure and specific volume are calculated from the measured shock and particle velocity data through the Hugoniot relations.

$$p = \rho_{oo} U u , \quad v = (1 - u/U) / \rho_{oo} , \quad (3)$$

with  $\rho_{oo}$  being the initial distended sample density. The calculated  $p - v$  Hugoniots for both densities are shown on the left in Figure (10) and exhibit some pertinent results. Shock compaction of a porous ceramic leads to excessive dissipative heating relative to comparable shock compaction of the full density ceramic. Shock heating would be substantially more so for the nominal 30% porous material than for the nominal 5% porous material. The relative extent of heating is observed, however, to be insufficient to separate the two sets of data in the pressure-volume plot through thermal expansion (Gruneisen) properties of the material. Where Hugoniot states for the two porosities overlap, pressure-volume values do not statistically differ. On the other hand, heating due to pore compaction is expected to markedly reduce residual strength at the shock state leaving material in a near hydrodynamic state (unable to support significant stress deviator). Strength states on the Hugoniot for near full density ceramic is an issue of current research and is pursued for boron carbide, for example, in the work of Vogler *et al.* [2004]. Further references on the same topic are collected in the ARL report of Dandekar [2001]. The lowest three Hugoniot points for the nominal 5% porous material appear to exhibit some strength on the Hugoniot, although it is known that the test method of McQueen *et al.* [1970] is not reliable at the lower shock amplitudes where structured shock waves are probably present.

The last observation, however, introduces an interesting point. Shock Hugoniot states achieved in near-full-density ceramic, which includes the work of Gust and Royce [1971], Grady [1994] and Vogler *et al.* [2004], do so through a structured shock wave. Hugoniot states are referenced from the Hugoniot elastic limit amplitude that is itself determined from the magnitude of a rather unusual, and probably unsteady, elastic precursor wave [Grady, 1994; Vogler *et al.*, 2004]. With the probable exception of the three lower points mentioned previously, because of material porosity, any elastic precursor wave is overdriven and transition to the Hugoniot state for the McQueen *et al.* [1970] data is through a single steady shock wave. This important difference may relate to some of the disparity in the high-pressure Hugoniot data for boron carbide ceramic.

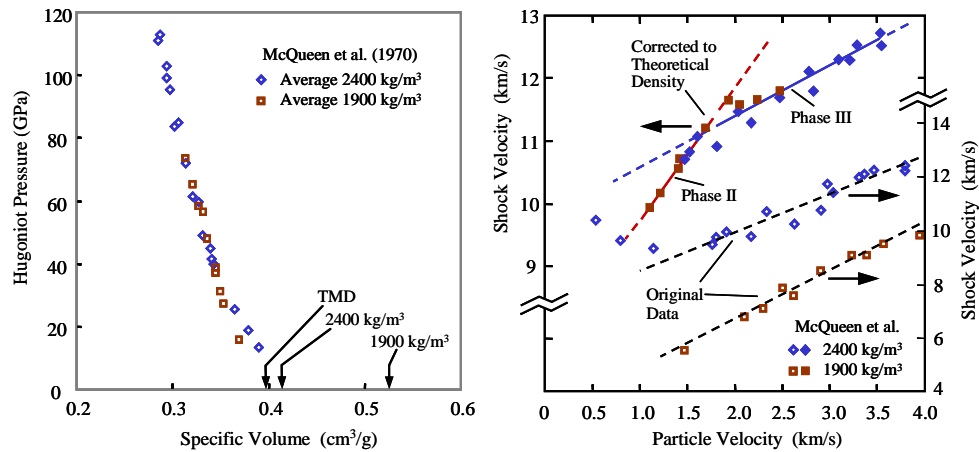


Figure 10: Shock Hugoniot data for boron carbide ceramic [McQueen *et al.*, 1970].

Synthesis of the two sets of the McQueen *et al.* Hugoniot data is capitalized on to assess sensitive high-pressure equation of state features of the boron carbide. The pressure versus specific volume Hugoniot data on the left in Figure (10) are mapped back into the more revealing shock velocity versus particle velocity plane through the Hugoniot relations,

$$U' = \sqrt{\frac{p}{\rho_o(1 - \rho_o v)}}, \quad u' = \sqrt{\frac{p(1 - \rho_o v)}{\rho_o}}, \quad (4)$$

where  $\rho_o = 2520 \text{ kg/m}^3$  is the theoretical density of boron carbide [Dandekar, 2001]. These shock velocity versus particle velocity states, shown as the solid symbols in the right hand plot in Figure (10), provide sensible shock velocity versus particle velocity Hugoniot states within the hydrodynamic equation-of-state surface (the hydrodynamic Hugoniot) for boron carbide referenced from the initial theoretical density.

With this normalization, the  $U - u$  data in Figure (10) display clear evidence for bi-linear behavior, indicative of a shock-induced phase change on the principal Hugoniot. The bi-linear curves shown in Figure (10) are the result of a statistical analysis of the data to determine the linear shock versus particle velocity constants for boron carbide phases identified as shock phase II and shock phase III in Table (2) and in the figure. All fits to the data provided a pressure intercept between 45 and 55 GPa (the shock transition pressure)

with the optimum  $U - u$  parameters in Table (2) intercepting closer to 45 GPa. The shock data is unable to distinguish between a second order transition (no transition volume change) and a small first order transition. A recent report of a shock transition in  $B_4C$  at 38 GPa with second order transition characteristics [Zhang *et al.*, 2006] is probably the same II-III transition identified here.

Table 2. Shock Phase Transformation Properties of Boron Carbide

Phase	$C_o$ (km/s)	$S$	$p_t$ (GPa)	$\Delta v_t$ (cm <sup>3</sup> /g)
$B_4C$ -I	9660	1.32	Ambient Phase	Ambient Phase
$B_4C$ -II	7700	2.15	25–35	$\approx 0.008$
$B_4C$ -III	9800	0.80	45–55	$<0.002$

A plot of the McQueen *et al.* [1970] Hugoniot data below 60 GPa is shown in Figure (11). The overlying curve is the linear  $U - u$  Hugoniot provided by  $C_o$  and  $S$  for phase II from the Figure (10) and provided in Table (2). As argued previously, the curve should provide a sensible estimate of the hydrodynamic compressibility of boron carbide within the stated range. There are some additional arguments for this conclusion. First, if there were a significant strength offset to the Hugoniot stress it would be highly fortuitous for the stress offset for the markedly different starting density materials to be the same. This argument would also support full compaction of the pore volume by the initial shock wave, and further suggests that local shear stresses are small compared to the compressive shock pressure. Second, and more convincing, elevated temperatures at the Hugoniot states for the more porous materials are inconsistent with significant material strength. In the range of 40 GPa shock pressure, containing a nice cluster of both 1900 kg/m<sup>3</sup> and 2400 kg/m<sup>3</sup> material Hugoniot points, temperatures of the lower initial density material subjected to Hugoniot shock compression are readily estimated. Based on a constant specific heat of 961.6 J/kg/K [Dandekar, 2001], an ambient average temperature rise due to shock heating is calculated to be about 2700 K. This level of temperature rise would approach the ambient melt temperature of boron carbide, which is also about 2700 K [Dandekar, 2001]. The specific heat can be expected to increase with temperature and therefore the calculated temperature rise is likely an overestimate. Nonetheless, it is unlikely that such temperature states on the Hugoniot would support significant material strength. Further, due to low thermal conductivity, it is also unlikely that thermal equilibrium on the microscale is achieved, leading to locally hot deformation regions that would additionally reduce material strength on the Hugoniot.

Manghnani *et al.* [2000] have measured ultrasonic properties of boron carbide to 2.1 GPa and determined a bulk modulus of  $K_o = 234.9$  GPa and the first pressure derivative  $K'_o = 4.26$ . These elastic constants, with a Murnaghan equation of state, are used to extrapolate compression to higher pressure. The extrapolated compression curve is shown on the right in Figure (11). Shock parameters  $C_o$  and  $S$  calculated from the reported  $K_o$  and  $K'_o$ , again

based on  $K_o = \rho_o C_o^2$  and  $K'_o = 4S - 1$ , are provided in Table (2) and correspond to the ambient boron carbide phase I.

It should be noted that a fairly broad range of ultrasonic wave speeds for boron carbide has been reported [Dandekar, 2001]. The reasons for this rather large disparity are presently unclear. It is suspected, however, that unusually low values are a consequence of microstructure effects (*e.g.*, crack porosity) and do not fully represent the lattice compressibility of the material. Measurements of Manghnani *et al.* [2000] were performed on a superior quality material, provided the highest ultrasonic values, and are considered closest to representing lattice compressibility properties of boron carbide.

The volume offset of the presumably hydrodynamic shock Hugoniot (as argued above) on the left in Figure (11), and the extrapolated ultrasonic compression curve suggests a further phase transformation within the pressure range of the data. It is unlikely that uncertainties in the Hugoniot data and the extrapolated ultrasonic compression curve could account for the 15-20% volume strain offset. As a caution, however, this offset is not reflected by the data of Gust and Royce [1971] and Vogler *et al.* [2004].

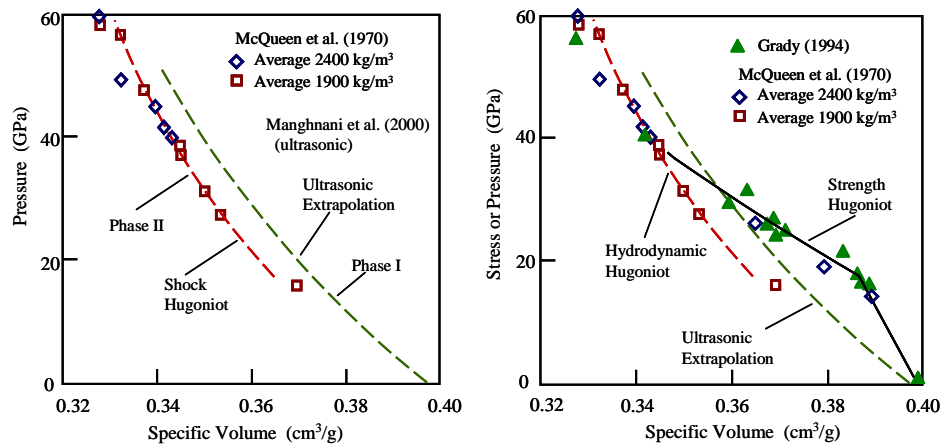


Figure 11: Experimental Hugoniot compression of boron carbide ceramic [McQueen *et al.*, 1970; Grady, 1994], and extrapolation of the ultrasonic compressibility of boron carbide [Manghnani *et al.*, 2000].

The transformation pressure at which the inferred phase change from  $B_4C$ -I to  $B_4C$ -II occurs is less certain. Structured shock wave profiles [*e.g.*, Grady, 1994] do not show clear evidence of a distinct transformation stress. The lowest pressure Hugoniot point on 1900 kg/m³ material of McQueen *et al.* [1970] at about 18 GPa suggests transformation from an ambient phase I to a shock phase II may have occurred under shock compression. Uncertainties in the single data point make this conclusion speculative, however. More recent analysis of earlier shock profile measurements on boron carbide using an alternative precursor echo analysis of the structured profile indicates wave profile anomalies above approximately 30 GPa shock pressure and transition to a more compressed state [Grady, 2002]. Thus, the shock profile data may also indicate phase transformation from a  $B_4C$ -I

phase (the ambient phase) to a  $B_4C$ -II phase (the shock phase II) at approximately 30 GPa, and suggest the range of 25-35 GPa provided in Table (2)

Shock Hugoniot data of Grady [1994] and the lowest three Hugoniot points for the 2400 kg/m<sup>3</sup> material from McQueen *et al.* [1970] are included on the right in Figure (11). The latter data are questionable because the experimental technique was not intended to apply to structured shock waves. Nonetheless, these data collectively illustrate that the Hugoniot strength of near-full-density boron carbide plays a role in this range of the data. The data provide a 15–20 GPa Hugoniot elastic limit for boron carbide ceramic and a Hugoniot strength offset to approximately 40 GPa. Agreement of the 40 GPa and 56 GPa Hugoniot states of Grady [1994] with the hydrodynamic phase II–III Hugoniot from the Marsh [1980] data suggest loss of strength on the higher pressure Hugoniot for this boron carbide ceramic. This observation was reported in an earlier study [Grady, 1994].

It is interesting to note, however, that the Hugoniot data of Gust and Royce [1971] and of Vogler *et al.* [2004] on near full density boron carbide ceramic are in sensible agreement with the McQueen *et al.* [1970] and Grady [1994] data up to Hugoniot pressures of about 30 GPa. Their data reside markedly higher (or to the right) above this pressure. The Hugoniot data of Vogler *et al.*, [2004] are shown with the latter data in Figure (12). A possible explanation is that dynamic strength and failure in the shock compression process have sensitivities to ceramic microstructure not yet understood. Such differences in behavior are hinted at by at least some of the precursor wave profiles measured in the study of Vogler *et al.* [2004], which exhibit stable deformation hardening unlike the marked stress relaxation observed in the comparable wave profiles reported in Grady [1994]. Clearly, further work is needed on the strength issue in boron carbide ceramic.

## *Hydrodynamic Equation of State*

Most computational models used in shock physics codes to capture the dynamic deformation of solids subjected to extreme loading conditions utilize an equation of state (here identified as a hydrodynamic EOS) to describe the mean pressure versus volumetric compression of the material. Distortional or shear strength of the material is captured through a separate model based on the deviator stresses. A description of the hydrodynamic EOS can be problematic, particularly when phase transitions are involved.

Unless a tabular description of the constitutive response is used, analytic relations must be incorporated to specify functional behavior of material compression and deformation. Compression of a material undergoing a phase transition, for example, is commonly described by a cubic polynomial to account for the material stiffening-softening-stiffening response through the transition region. Empirical polynomials are approximations at best, pathological outside the range of the data fit, and, where wave propagation is involved, incur additional difficulties where sensitivity to the local derivative of the polynomial is critical.

More appropriate is to make use of physically measured material constants when available. The shock-velocity-particle-velocity constants for the three phases are such appropriate

constants for boron carbide. These constants provide the hydrodynamic compression of each phase as is illustrated by the dashed curves in Figure (12). Remaining then, is an appropriate analytic expression for phase transformation from one phase to the next. A reasonable approach is to provide a specific volume versus pressure relation for each phase, utilizing the appropriate  $C_o$  and  $S$  constants, and express the transformation through a composite relation,

$$v(p) = (1 - \lambda)v_I(p) + \lambda v_{II}(p), \quad (5)$$

In this relation  $\lambda(p)$  is a pressure dependent transformation parameter defined over the interval  $0 \leq \lambda \leq 1$  that affect the transition from phase I to phase II. In principal any functionally appropriate form for  $\lambda(p)$  that captures the transformation features can be used. One convenient form is the exponential expression,

$$\lambda(p) = 1 - e^{-(p/\sigma)^n}. \quad (6)$$

A more detailed description of such physics-based hydrodynamic equations of state has been provided in Grady [2002]. The solid curve shown with the data in Figure (12) is the result of such an effort.

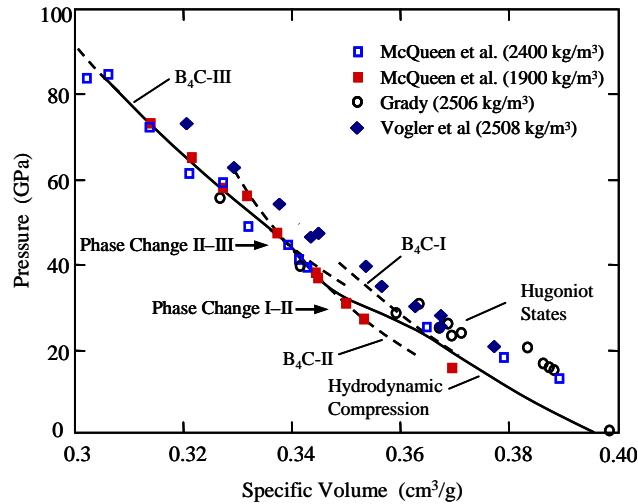


Figure 12: Experimental Hugoniot data and the model representation of the hydrodynamic Hugoniot compression of boron carbide.

Such an analytic representation of the hydrodynamic compression of boron carbide requires considerably more material constants than say an empirical cubic relation, which could probably adequately fit the McQueen *et al.* [1970] data within experimental uncertainty. It is argued, however, that the present analytic description has a stronger physical basis, and that material constants have a more transparent origin, in the underlying shock wave and static high-pressure experiments. Further, more confidence can be placed on derivatives of the analytic relation essential to wave propagation in the material.



Accepting the physical interpretations of the shock data leading to the hydrodynamic equation of state for boron carbide displayed in Figure (12), uncertainties ascribed to this EOS are less than  $\pm 2\%$  in volume strain.

Also included in this final plot are additional Hugoniot data for boron carbide ceramic from the more recent study of Vogler *et al.* [2004]. There is reasonable agreement among all of the higher density material Hugoniot states to shock pressures of about 25–30 GPa. At higher pressures the Hugoniot data of Vogler *et al.* [2004] reside well above (or to the right of) the data of McQueen *et al.* [1970]. A tempting explanation is that strength on the Hugoniot accounts for the marked difference, and this may be. One difficulty with this explanation, however, is that the two Hugoniot points of Grady [1994] in the neighborhood of 40 and 55 GPa, also on a high-quality near-full-density ceramic, are in agreement with the McQueen *et al.* [1970] data and differ markedly from that of Vogler *et al.* [2004]. As noted earlier, more work is required before the shock wave properties of boron-carbide ceramic are fully understood.

## Strength Under Shock Compression and Static Scaling Studies

Recent static strength measurements on boron carbide have important implications to computational modeling of this ceramic in the impact shock and ballistic environment. Some background discussion is warranted. The strength data shown in Figure (13) has been reported [Kirkland *et al.*, 2009; Wereszczak *et al.*, 2009]. These data provide a striking demonstration of size scale dependence of boron carbide ceramic strength. In this plot, size is identified as an effective sample area subjected to the strength test. Several dynamic strength measurements for boron carbide obtained from shock wave tests are included on the same plot.

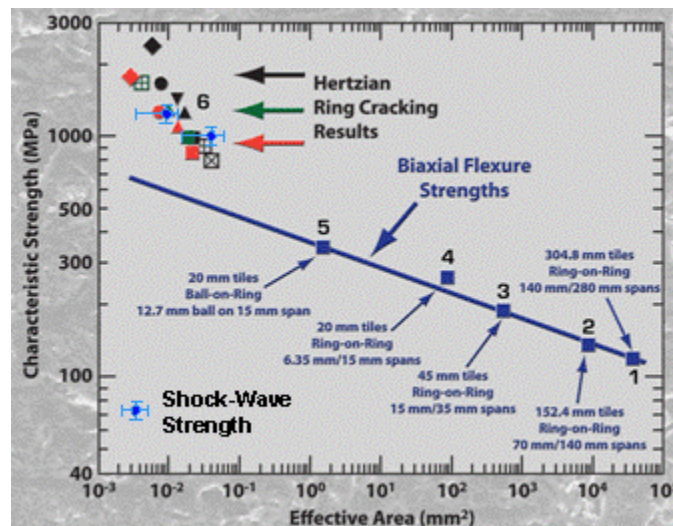


Figure 13: Scale dependence of boron carbide strength [Kirkland *et al.*, 2009; Wereszczak *et al.*, 2009] and comparison with shock wave strength assessed for Hugoniot elastic limit measurements.

The relationship of these static strength data and strength measurements from shock wave data are not immediately apparent. The most common means for extracting strength from a shock profile measurement is through assessment of the elastic precursor wave preceding the deformation shock wave that carries the material to the final shock compressed state. The strength measure extracted from the precursor wave amplitude is referred to as the Hugoniot elastic limit. Precursor waves as part of a structured shock wave can be complex. The assessment of strength and the processes of inelastic deformation associated with the precursor signature can be equally complicated.

Wave profiles for boron carbide ceramic are provided in Figure (14) that shows the precursor wave from which the Hugoniot elastic limit (HEL) strength is assessed. Hugoniot elastic limits of 17 GPa and 21 GPa are identified in the figure. The HEL is observed to depend on the amplitude of the impact shock wave. Using the elastic Poisson's ratio for boron carbide, a dynamic yield strength of 10 GPa and 12 GPa are calculated for the lower and the higher shock amplitudes, respectively.

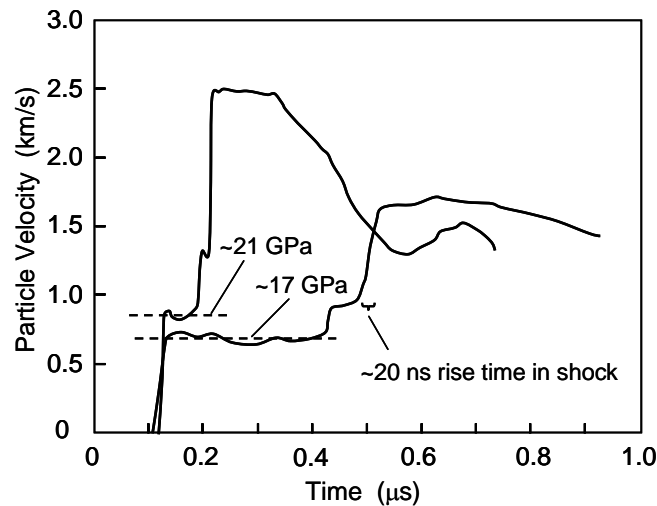


Figure 14: Shock wave profiles for boron carbide ceramic illustrating dependence of strength on shock amplitude [Grady and Moody, 1996].

To compare the shock strength of boron carbide ceramic with the static strength versus size scale behavior plotted in Figure (13), an estimate of the sample size tested in the shock wave experiment must be assessed. Dynamic failure and the strength at which failure occurs is established in the shock wave following the elastic precursor wave. The risetime of the shock wave provides a characteristic time over which shock failure occurs and, concurrently, through the local sound speed, establishes the region of material that cooperatively participates in the failure event.

A risetime of approximately 20 ns is identified for the lowest amplitude shock wave profile shown in Figure (14). This risetime is well within the resolution limits of the VISAR instrumentation used to record the profiles. Assuming a sensible sound speed of 10 km/s, a shock thickness of about 0.2 mm is calculated. Squaring this value provides an area measure of approximately 0.04 mm<sup>2</sup> for the shock region participating in the failure process and for

which the shock strength is assessed. A dynamic yield of 10 GPa and area of 0.04 mm<sup>2</sup> is plotted in Figure (13) and found to be in good agreement with the static strength data [Kirkland *et al.*, 2009; Wereszczak *et al.*, 2009].

The risetime of the higher amplitude shock wave is less than the resolution of the VISAR instrumentation. An estimate of the shock risetime and the effective sample area is provided by assuming a relation, commonly referred to as the fourth-power law [Swegle and Grady, 1985], that provides the dependence of shock risetime on shock amplitude for a wide range of materials. This assumption provides an area measure of approximately 0.01 mm<sup>2</sup> for the higher amplitude shock wave. This higher amplitude shock strength is also plotted in Figure (13).

The agreement between the dynamic strength assessed from shock wave measurements and the size scaling of static strength obtained from several test methods for boron carbide ceramic has implication to strength modeling of the material. Strength is also known to depend on the state of confining pressure and the strain rate, among others. These latter strength dependent effects appear to be second order relative to size scaling for boron carbide.

Through the analysis performed, it is clear that time and size scale are intimately related through the material sound speed. The observed strength behavior suggests the need for a time, or history, dependent strength model. One such model that has been described in earlier reports is the Tuler-Butcher failure criterion [Tuler and Butcher 1968].

The time and size scale dependence exhibited by boron carbide can be expected in other highly brittle solids. Glass and glass ceramics would be suspect in this regard. There are a number of other ceramics that do not exhibit the same time and amplitude dependence of shock strength. Examples include aluminum oxide, silicon carbide and tungsten carbide. Comparable static size scaling studies on these ceramics would be of interest.



## V Fragmentation in the Ballistic Event

The catastrophic disruption of materials in the ballistic environment commonly plays a central role in both the successful application of armor systems and the effective application of anti-armor systems. A theory of the dynamic fragmentation of solids based on continuum energy principles has provided a basis for assessing fragmentation in a wide range of ballistic applications over the past several decades [Grady, 1982; 1988; 2009]. Applications of the theory to the fragmentation of brittle solids, including glass and ceramic, have been problematic, however. Recently, some of the physics issues governing length scales and size distributions in the dynamic fragmentation of brittle solids have come to light. The earlier energy-based fragmentation theory has been broadened to accommodate dynamic fragmentation in brittle materials. This section summarizes past theories and their applications to fragmentation in the ballistic environment.

More recent applications to ballistic fragmentation of glass and ceramic materials are described. Additionally, recent edge-on glass impact experiments lends insights into the time-dependent fracture wave phenomenon. A cursory exploration of these data is undertaken in the context of fracture wave propagation.

### *Fragmentation Ductile and Brittle Solids*

Fragmentation of the component materials is a natural consequence of a terminal ballistic event. Commonly, the size distribution and trajectory of the resulting fragment debris is central to the effective application of the projectile or armor component specific to the event.

The multiplicity of materials of interest in terminal ballistic applications spans a wide range of breakup and fragmentation phenomena. The catastrophic fragmentation of brittle solids under the intense dynamic loading of the ballistic event is particularly interesting, and is perhaps the least understood.

The focus of this discussion is on the dynamic fragmentation of brittle solids with particular emphasis on ceramic and glass. A theory of dynamic fragmentation for brittle materials is proposed. This theory is not a model of fragmentation for any specific application. Rather, the theory draws on underlying physical principles that determine the functional forms of the analytic relations that describe of the statistical fragment size distributions and the fragmentation size length scales.

The section provides some necessary background on the topic of dynamic fragmentation of solids necessary to the extension to brittle solids. Previous theoretical work is outlined that is pertinent to the present theoretical progress to brittle solids. The seminal wartime contributions of Nevill Mott [Mott 1943; 1947] to the area of dynamic fragmentation, integral to the progress, are recognized.

## Mott Fragmentation

In the study of the dynamic fragmentation of solids there are several historical threads that can be traced. For those concerned with the topics of terminal ballistics, or exploding munitions, the seminal wartime effort of Nevill Mott [*e.g.*, Mott, 1943; 1947] is by far the most relevant. Of the several early efforts at achieving a theoretical understanding of dynamic fragmentation, the work of Mott has the more solid physical basis. The fragmentation theory of Mott predicted the two key elements of the dynamic fragmentation event. Namely, the statistical distribution in fragment size, and the governing distribution length scale or, equivalently, the average fragment size.

A feature of Mott's seminal theoretical study of fragmentation that has become a part of the lore in representation of terminal ballistics or exploding munitions fragmentation is the fragment distribution Mott plot. The Mott plot is a representation of the fragment distribution of a specific fragmentation event where the logarithm of the cumulative fragment number larger is graphed against the individual fragment mass, that is,  $\ln N = f(m)$ . Often the data plot linear, or near linear, in this representation of the fragment size data. Some may contend that the Mott plot more specifically implies log number versus some particular power of the fragment mass. Mott himself vacillated on this point and, in one of his later wartime reports, suggested that a linear dependence on the mass  $m$  is perhaps the most appropriate. In any case, a Mott plot is here defined as a semilog plot of the cumulative fragment number versus mass or,  $\ln N$  versus  $m$ . The fragment size data do not always plot linear, but this representation is an appropriate space for a clear display of a broad body of dynamic fragmentation data.

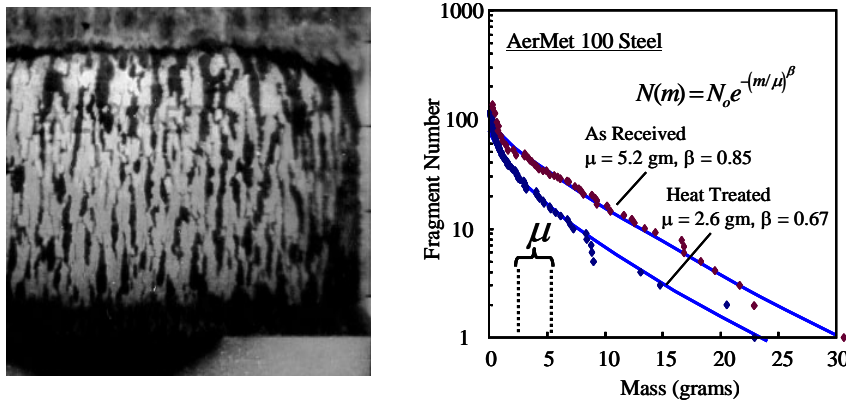


Figure 15: Mott fragmentation plots for two explosive tests on AerMet-100 steel cylinders and high-speed photograph of representative test [Chhabildas *et al*, 2001].

Mott was principally concerned with a theoretical description of fragmenting munitions and expended most of his efforts in describing the breakup of an explosion-driven expanding cylindrical case. The Mott plots for several such case fragmentation experiments performed on AerMet-100 steel cylinders and a high speed photograph of one fragmentation event [Chhabildas *et al*, 2001] are shown in Figure (15).

A Mott plot representation is found to provide a useful description of fragment distributions resulting from a wide range of disparate fragmentation events [e.g., Grady, 2009]. Further examples are provided later. Statistical arguments are given to show why this is the case.

## Brittle Fragmentation

As pointed out in the previous subsection numerous applications in dynamic fragmentation are well displayed in the Mott plot representation of the distribution data, or, a plot of log cumulative number versus fragment mass. There are examples, however, of dynamic fragmentation where a Mott plot representation is not appropriate. Fragmentation of highly brittle materials, and perhaps other materials, results in fragment distributions that are poorly displayed on a Mott plot. Fragment fines are so numerous that counting fragments is not reasonable. Sieving techniques are used to separate fragments into size ranges. Fragment distributions are most commonly represented through plots of cumulative mass versus fragment size. Such distributions are observed to plot linear or near linear in a log cumulative mass versus log size display, or Schuhmann distribution [Schuhmann, 1940], of the fragment size data. There are many examples of fragmentation of brittle materials that would make the salient points. An example is chosen here because of direct relevance to the terminal ballistics effects of interest.

The example is that of tests in which plates of boron carbide and composite are subjected to normal impact by tungsten carbide core armor piercing projectiles. Of interest here is the shatter fragmentation of the boron carbide ceramic. The authors of this study [Moynihan *et al*, 2002] collected and determined size distributions for the resulting boron carbide fragment debris. Fragment distributions plotted in the Schuhmann form are constructed from the data and are shown in Figure (16) from tests for several impact velocities. The near linear plots with power of order unity are representative of the behavior of brittle materials. Broadly, the power  $n$  ranges over about  $0.5 < n < 1.5$ , and occasionally higher, in Schuhmann plots of brittle fragment distribution data.

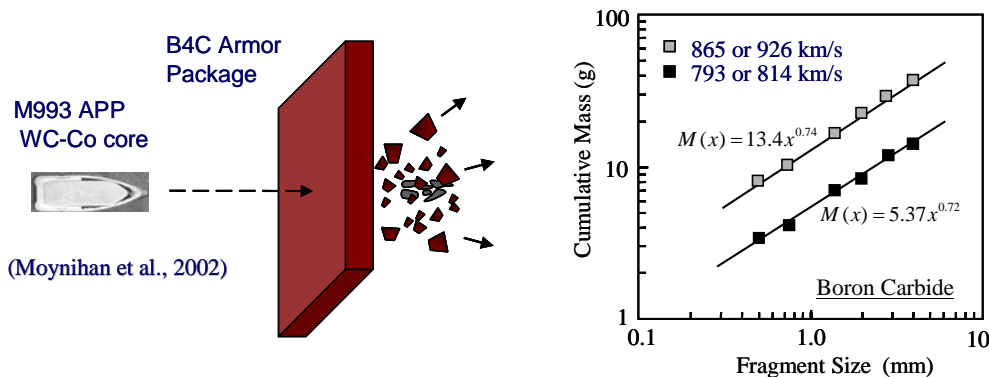


Figure 16: Schuhmann fragment size distribution plot constructed from data for boron carbide ceramic subjected to ballistic impact by tungsten carbide core projectiles [Moynihan *et al*, 2002].

## Equilibrium Fragmentation

Before assessing the physics of fracture and fragmentation of brittle solids, a description of a theory of dynamic fragmentation is necessary that has demonstrated reasonably success for other materials. A representative set of test data that will be examined in describing this theory is shown in Figure (17). In these tests the behind target fragment debris was captured and analyzed. The fragment size distribution Mott plots are shown for two tests from a series of experiments in which plates of stainless steel were subjected to impact by copper spheres over a selected range of impact velocities and angles of obliquity [Grady *et al.*, 1996].

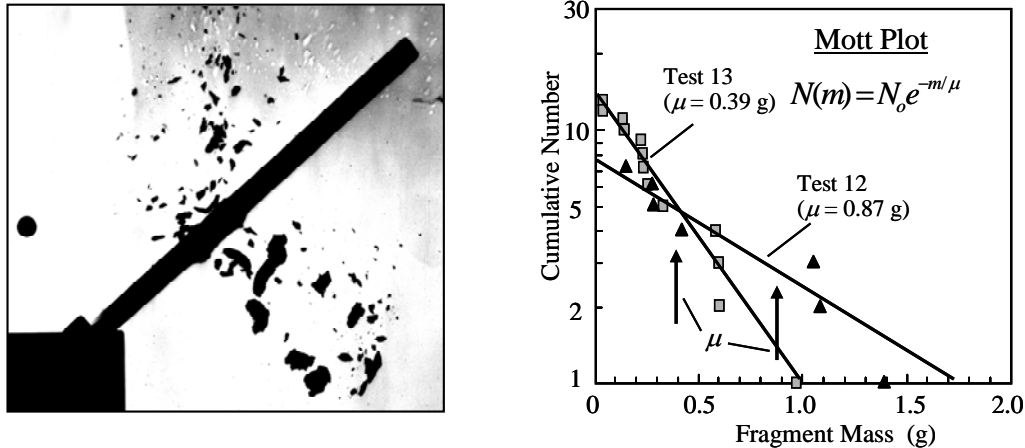


Figure 17: Impact of a copper spheres onto stainless steel plates [Grady *et al.*, 1996]. Mott plot of the behind target fragment distribution for two such tests. Impact angle from normal, and velocity: Test 12, 60 degrees, 3.26 km/s; Test 13, 50 degrees, 3.09 km/s.

As the fragmentation theory is described, reference will be made to equilibrium and nonequilibrium fragmentation. Briefly, equilibrium or nonequilibrium refers to the ability, or lack thereof, of the material to undergo fracture failure and fragmentation when a theoretical energy criterion is achieved. An energy criterion identifies onset of equilibrium fragmentation. Delayed failure and an additional failure criterion exemplify nonequilibrium fragmentation. At the present state of understanding, equilibrium fragmentation appears to have fairly broad application across a range of material types. Nonequilibrium fragmentation applies to the brittle materials such as the competent ceramics and glasses. Some form of continuous transition from equilibrium to nonequilibrium fragmentation seems reasonable, however the boundaries of departure from one to the other are still poorly understood.

The fragment size distribution data for the two tests shown in Figure (17) are sensibly described by a simple exponential, or Mott, function of the form,

$$N(m) = N_0 e^{-m/\mu}. \quad (7)$$

The fragment size scale factor  $\mu$  is observed to decrease as the intensity of the impact increases. In other words, higher velocity impact results in more, but smaller, fragments.



The theory, and sought for physical understanding, is focused on two key elements; first, prediction of the distribution of fragment size resulting from the event; second, prediction of the distribution size scale  $\mu$  and its dependence on the impact intensity and material properties.

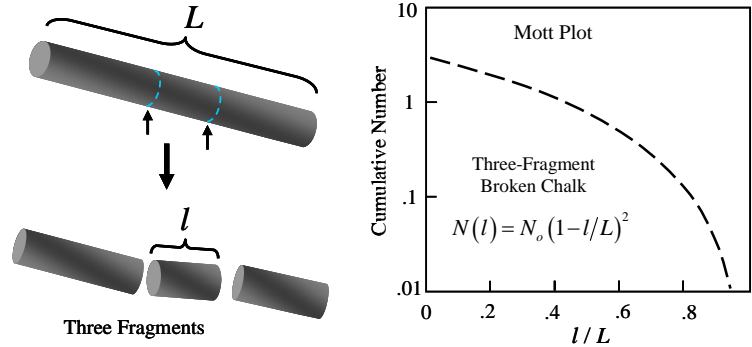


Figure 18: Length  $L$  is broken into three fragments with equal likelihood of fracture placement. The fragments size distribution Mott plot resulting from a binomial probability is shown on the right.

### Fragment Size Distribution

I have heard a tale that if a stick of blackboard chalk (actually pressed gypsum in the later years of chalk and blackboard use) is dropped onto the floor, it breaks invariably into three pieces. (In today's increasing use of grease pencils and white boards, this tale is rapidly becoming dated.) Whether true or not, it provides a theme for this first look at fragment size distributions. The chalk of length  $L$  in Figure (18) is broken at two places that are assumed to have equal likelihood of occurrence at any point within the length. The distribution of possible fragment sizes is governed by binomial statistics and yields the cumulative probability distribution for fragments of length  $l$  of the form [Grady, 1990; 2006],

$$F(l) = 1 - (1 - l/L)^2. \quad (8)$$

The corresponding Mott distribution ( $N_o = 3$ ) is shown in Figure (18). If the number  $n$  of fragments that the length  $L$  is partitioned into is increased, the curve in the Mott plot becomes increasingly linear and in the limit, the fragment distribution approaches the exponential form,

$$N(l) = N_o e^{-l/\lambda}, \quad (9)$$

where  $\lambda = L/n$  is the average fragment length. Equation (9) is derived directly if an unbounded length is fractured along the length with frequency  $\lambda$ , in which case the fragment size distribution is determined from Poisson probabilities.

The present one-dimensional model results in an exponential distribution in fragment sizes not unlike the experimental results provided in Figure (17). One is encouraged to explore the random geometric fragmentation problem in two, and perhaps three, dimensions. Various early workers in the field have undertaken investigation of random geometric fragmentation and its possible application to real fragmentation. Mott and Linfoot (1943) pursued one approach in their initial report on munitions fragmentation. Some of this history is provided in a recent review [Grady, 2009].

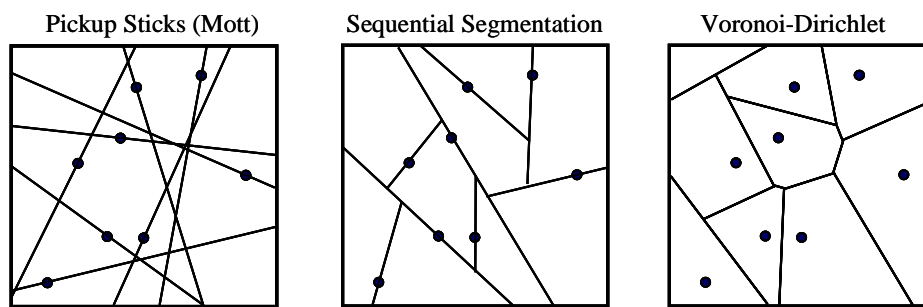


Figure 19: Three algorithms for randomly fragmenting a surface.

Consider random fragmentation in two dimensions. One immediately confronts a problem not evident in the random fragmentation of a line. Namely, a decision is necessary as to what form of algorithm to use in randomly partitioning the surface. Three of many possibilities are illustrated in Figure (19). Each algorithm starts through random placement of points on the surface. In the first, lines are scribed through the surface with random orientation. This fragmentation algorithm was investigated by Mott and Linfoot (1943) in some detail. For obvious reasons the algorithm has been identified as pick up sticks fragmentation. In the second algorithm randomly oriented lines are sequentially scribed through the points that bisect the entered fragment. Third is the well-known Voronoi tessellation. Analytic expressions for the fragment size (area) distributions have been determined for each of the fragmentation algorithms, although some intuitive license is applied in one instance [*e.g.*, Grady, 2009]. The pick-up sticks algorithm results in a Bessel function distribution of the fragment sizes. Sequential segmentation is exactly described by a simple exponential. The Voronoi tessellation provides a gamma function fragment size distribution. The Mott curves for each of the algorithms are compared in Figure (20).

Notably, much of the distribution for the three algorithms is nominally the same. It is only for a reasonably small fraction of the total at the small fragment tail of the distribution that the curves differ. The Voronoi algorithm results in a dearth of small fragments whereas the pick-up sticks algorithm leads to an excess.

One can speculate, based on the three examples, that random geometric fragmentation of a surface, and by extrapolation a volume, will result in an exponential functional form with a single size scale parameter, although not necessarily a simple exponential. Further, the distribution is reasonable insensitive to the fragmentation algorithm (discounting the small fragment tail).

The cumulative probability distribution for each of these examples can be written,

$$F(m) = 1 - e^{-\int_0^{m/\mu} h(\xi) d\xi}, \quad (10)$$

where the likelihood function  $h(m/\mu)$  will differ for each of the examples. The key point is that each of the distributions is constrained by a single length (size) scale  $\mu$ , which provides the scale factor for the distribution.

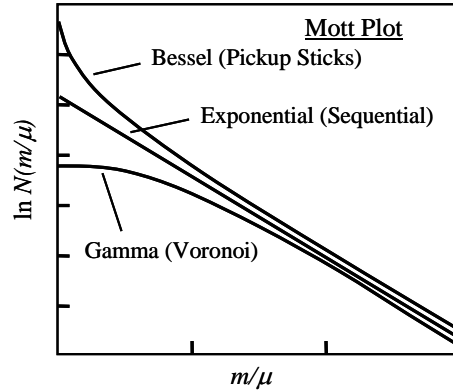


Figure 20: Fragment size distributions in Mott plot representation for three fragmentation algorithms.

The preceding efforts have, of course, been an exercise in geometric fragmentation where a Poisson point process followed by a partitioning algorithm is used to randomly fragment a body. The dynamic fragmentation of many materials does not markedly differ from this geometric process, however. Dynamic spall in metals, for example, as exhibited by the images provided in the reviews of Shockey *et al.* (1973) and Curran *et al.* (1987), are processes in which fractures activate at random at independent points in the body, accelerate, grow, and ultimately coalesce to provided surfaces of the fragmented material. Physics-based models with increasing degrees of sophistication governing random fracture activation, growth and coalescence result in fragment distributions of the form provided in Equation (10).

The classic physics-based fragmentation model of Mott (1947) is a one-dimensional analysis undertaken to determine the distribution in spacings resulting from the axial splitting of explosively expanding munitions. The resulting distribution is of the form of Equation (10) with a power-law likelihood function  $h(m) = (m/\mu)^\beta$ . In the Mott model and analysis the resulting size scale is shown to be approximately  $\mu \propto \sqrt{\rho Y / \gamma \dot{\epsilon}}$ , while the power is about  $\beta \approx 7/2$ . The material density and yield stress are  $\rho$  and  $Y$ , respectively,  $\dot{\epsilon}$  is the strain rate of the expanding munitions, while  $\gamma$  is the Mott statistical fracture parameter [Mott, 1947; Grady, 2006].

These theoretical arguments, although not definitive, support the exponential or near exponential character observed in many of the dynamic fragment events where a single size scale parameter ties the distribution to the intensity of the event. Remaining then, is an

assessment based on theoretical considerations of this size scale factor for a given dynamic fragmentation event.

### *Fragment Size Scale Factor*

Again, the impact fragmentation experiment depicted in Figure (17) will provide the application for a theoretical assessment of the scale factor constraining the experimental fragment size distribution. Impact causes the dynamic fragmentation of a portion of the plate neighboring the point of impact. The fragment debris is ejected and expands with an intensity that is proportional to the impact velocity. If the impact velocity is increased the number of fragments produced is greater and the average fragment size is smaller. The scale factor in the exponential expression for the fragment size distribution accounts for the dependence on intensity of the fragmentation event.

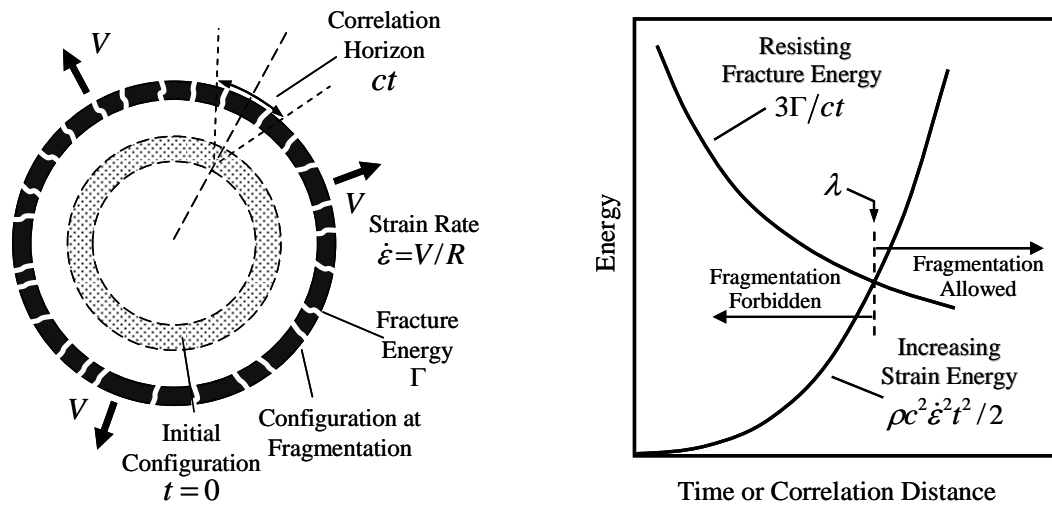


Figure 21: Model for visualizing the energies governing the characteristic fragment size in an equilibrium fragmentation event.

The principle issues concerning the fragmentation process in this example are captured in the idealized, but conceptually more transparent, model illustrated in Figure (21). A thin circular ring, or a spherical shell, of material is provided an initial impulse leading to a symmetrically outward expansion at a velocity  $V$ . (Deceleration due to deformation dissipation of the initial kinetic energy is ignored.) A sensible measure of the expansion intensity is provided by the expansion rate  $\dot{\epsilon} = V/R$ , where  $R$  is the radius of the ring or shell. If material deformation response to the imparted motion is linear elastic, then elastic strain energy increases with time according to,

$$U_e = \rho c^2 \dot{\epsilon}^2 t^2 / 2, \quad (11)$$

where  $c$  is an appropriate elastic wave speed that determines the elastic modulus of the material. After onset of expansion, this wave speed also determines a correlation horizon [Grady, 1988]. This correlation horizon determines at any time  $t$  a region of the material in which material points are within an elastic communication distance. Within the correlation

horizon, elastic stresses can adjust to modest variations in elastic modulus and concentrate stresses at points of weakness. A fundamental, and logically reasonable, precept of the theory is that, if fragmentation occurs within a time  $t$ , then fragments can be no larger than the region determined by the correlation horizon  $ct$ . A straightforward calculation provides a lower-bound fracture surface energy density over the body of,

$$U_s = 3\Gamma/ct, \quad (12)$$

where  $\Gamma$  is the fracture surface energy per unit area generated in the event. For example, if the body is a metal with fracture toughness  $K_c$ , then a reasonable estimate of the fracture energy is provided by  $\Gamma \approx K_c^2/2\rho c^2$ .

A plot of both the elastic strain energy in Equation (11) that will fuel the fracture process, and the resisting fracture energy in Equation (12) that will be supplied by the strain energy, are plotted as a function of the correlation distance (or time) on the right of Figure (21). The correlation horizon as the body expands is also illustrated in the picture on the left. The strain energy is for this example an increasing quadratic function of time. The resisting fracture energy required to fragment the body is correspondingly a decreasing function of time. Fragmentation is not allowed until the energies are equal. Equality occurs at a correlation distance identified as  $\lambda$  in the figure. Although certainly not required, an assumption of the present energy-based theory is that equilibrium fragmentation occurs when the two energies are nominally equal and the correlation length  $\lambda$  provides the scale factor constraining the fragment size distribution. For the exponential distributions describing the fragment size data in Figure (17) the mass scale is  $\mu \approx \rho\lambda^3$ .

By equating the energy relations provided in Equation (11) and (12), an analytic expression,

$$\lambda \approx \left( \frac{6\Gamma}{\rho\dot{\epsilon}^2} \right)^{1/3}, \quad (13)$$

for the governing fragment size length scale is directly calculated from both fracture properties of the material and a strain rate measure of the intensity of the fragmentation event. Application of Equation (13) to the tests provided in Figure (17) based on properties for stainless steel and kinematic properties of the fragmentation event provide size scale factors that are in remarkably good agreement with the experimental results. Similar successes of the theory have been demonstrated in numerous other applications in dynamic fragmentation [Grady, 2009].

## Nonequilibrium (Brittle) Fragmentation

Nonequilibrium fragmentation, in contrast to equilibrium fragmentation, occurs in those materials that, when subjected to dynamic fragmentation conditions appropriate to the plot in Figure (21), do not fail at the juncture of the two energy curves. Instead, elastic strain energy continues to increase until some other failure criterion is achieved. In the present context,

this behavior applies to glass and to certain very brittle ceramics such as boron carbide. As noted earlier, nonequilibrium fragmentation most probably occurs to some extent in numerous other materials. This interpretation of the energy-based fragmentation theory is less mature and has not yet been extensively explored [Grady, 2008; 2009].

### *Theoretical Basis*

The comparable energy plot for nonequilibrium fragmentation is illustrated in Figure (22). When strain energy is achieved that is necessary to fuel the required fracture energy, all conditions sufficient for failure and fragmentation are not present. Strain energy, correlation length, and time continue to increase until an alternative criterion is achieved that provides both the necessary and the sufficient conditions for failure.

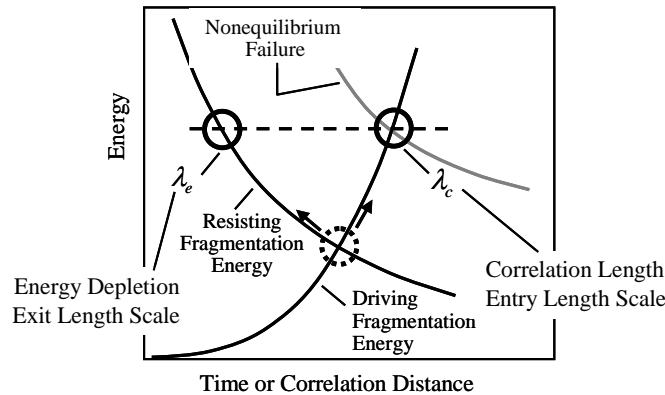


Figure 22: Nonequilibrium conditions leading to a schism in length scales spanning the fragment size distribution in brittle solids.

An application of nonequilibrium fragmentation perhaps most easily visualized is that of spall in glass. In the spall process release waves interact and carry regions of the glass into tension at a high rate of strain (of order  $10^5/s$  to  $10^6/s$ ). Because of the very modest energy required to create new fracture surface in glass, strain energy necessary for failure and fragmentation occurs at a tension of a few tenths of a GPa. Experimental studies show, however, that tensile stresses in the neighborhood of several GPa (one order of magnitude higher) are achieved before the spallation of glass. Reasons for the markedly high spall strengths of glass presumably relate to the very modest defect structure in the material, and the stress and stress correlation states that must be achieved to activate internal cavitation.

Although more complex, similar nonequilibrium fragmentation governs failure in the ballistic impact tests on boron carbide ceramic target plates for which the fragment size distribution data are shown in the previous Figure (16). Namely, elastic strain energy achieves levels that far exceed the required fracture energy before failure and fragmentation proceeds. Again, the material defect structure, joined with the elastic strain energy and strain energy history, combine to determine the elevated nonequilibrium state at which failure begins.

The correlation length scale  $\lambda_c$  at onset of failure determines the initial fabric of fracture. Fractures on a spacing of this characteristic length scale, however, are not sufficient to dissipate the excess elastic strain energy stored in the body preceding failure. Fracture failure proceeds through successive crack branching until available strain energy is exhausted and a fracture fabric is achieved commensurate with the fracture surface energy length scale  $\lambda_e$  identified in Figure (22).

In summarizing to this point, certain competent brittle solids do not exhibit equilibrium fragmentation governed by a single length scale  $\lambda$  occurring at the juncture of the elastic strain energy and fracture resistance energy curves as shown in Figure (21). Such brittle solids instead exhibit nonequilibrium fragmentation governed by an alternative, markedly higher energy, failure criterion that leads to a schism in length scales as illustrated in Figure (22). The correlation length scale  $\lambda_c$  and surface energy length scale  $\lambda_e$  can be decades apart in highly nonequilibrium dynamic fragmentation applications.

Much of the dynamic fracture and fragmentation physics is enveloped by the surface fracture energy and correlation length scales  $\lambda_e$  and  $\lambda_c$ . Onset of failure and initial fracture is governed by the correlation length scale  $\lambda_c$ . Continued fracture, through successive crack branching, cascades down through the length scales until strain energy is exhausted at the length scale  $\lambda_e$ . Over a range of length scales bounded by  $\lambda_e$  and  $\lambda_c$ , the physics of fracture is independent of length scale. Physical processes become self-similar within this range and physical symmetry dictates that such processes are described by power-law functions of the length scale  $\lambda_e < x < \lambda_c$ . The general concepts have application to other areas of physics including hydrodynamic turbulence [Falkovich and Sreenivasan, 2006] and fatigue fracture [Barrenblatt, 2006]. This physics is commonly referred to as a *law of intermediate asymptotics*.

In particular, within this range of length scales the resulting distribution of fragment sizes is necessarily power-law. Expressed as a cumulative fragment number distribution greater than size  $x$ , the distribution is written in the form,

$$N(x) \propto x^{-d}, \quad (14)$$

where the exponent  $d$  is the fractal dimension of the distribution [Turcotti, 1986]. The distribution is readily transformed to the Schuhmann mass distribution,

$$M(x) = M_0 x^n, \quad (15)$$

where the Schuhmann index  $n$  is related to the fragment size fractal dimension [Turcotti, 1986] through  $n = 3 - d$ . A complete fragment distribution spanning the upper and lower length scales would, of course, be functionally more complex, but must be asymptotic to power-law behavior in the intermediate range.

The energy-based theory of nonequilibrium fragmentation provides a qualitative explanation for the ballistic impact generated fragment size distribution for boron carbide ceramic shown in Figure (16), as well as many other applications of dynamic fragmentation of brittle solids. The data are clearly described by a power-law function that span a finite range of fragment sizes. A more quantitative assessment of fragmentation requires both a clearer description of the impact conditions and a criterion for failure under the dynamic loading imposed.

### Experimental Observations

The fragment distribution data from Figure (16) for ballistic impact tests on boron carbide ceramic [Moynihan *et al.*, 2002] are repeated in Figure (23), and compared with a qualitative description of the fragment distribution inferred from the theory. The character of the experimental fragment size distribution is in sensible agreement with the predicted theoretical behavior. The measured sieve data are consistent with a power-law distribution. It can be safely inferred that the experimental distribution exhibits an upper and lower bound.

A number of further questions, however, are raised concerning the theory. How are the correlation and energy length scales that determine the range of power-law behavior calculated? What is the appropriate dynamic failure criterion in the nonequilibrium fragmentation event? What properties of the material and/or the fragmentation event determine the exponent  $n$  in the power law? What is the span of the power-law range? Although not yet fully understood, these and related issues are discussed in the closing topics of this section.

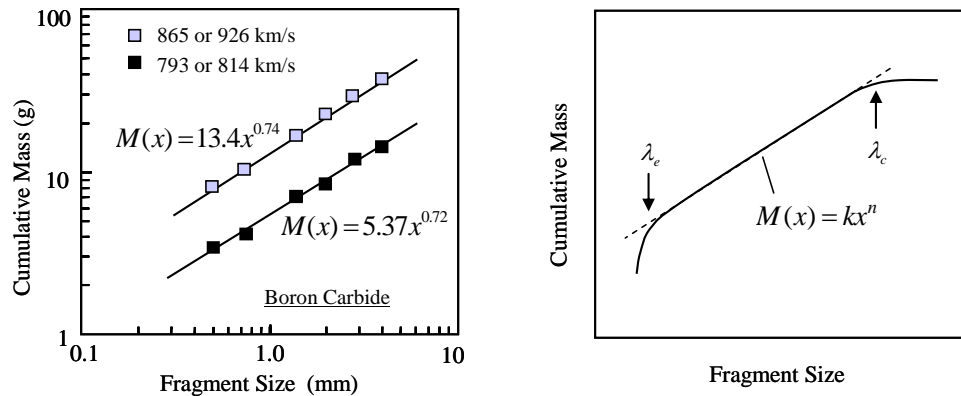


Figure 23: Experimental fragment size data for boron carbide ceramic [Moynihan *et al.*, 2002] and a qualitative comparison with the functional character of the nonequilibrium fragmentation theory.

### Brittle Failure Criteria

Energy-based fragmentation of brittle solids under equilibrium conditions provides a failure criterion firmly founded on commonly available properties of the materials. Failure occurs at the juncture of the elastic strain energy and fracture energy curves shown in Figure (22), allowing direct calculation of the governing fragment size length scale as well as both the time and stress to failure under the loading conditions imposed.



Nonequilibrium fragmentation enters a realm in which the failure properties of brittle solids are not well understood. In the brittle solids of interest, elastic strain energies under the loading conditions imposed achieve dynamic levels that far exceed equilibrium values before failure and subsequent fragmentation occurs. Failure activates at internal or surface sites of weakness under stress and time conditions that are not yet fully understood. A first-order assessment of the Figure (16) boron carbide experiments within the present fragmentation model is achieved by assuming that a nonequilibrium elastic strain energy commensurate with the Hugoniot elastic limit ( $\sigma_{hel} \approx 15$  GPa) is attained within approximately one transit of the plate thickness before failure and fragmentation proceeds. These conditions would place the correlation length scale  $\lambda_c$  of the order of the plate thickness ( $\lambda_c \approx 5$  mm). The lower energy length scale is calculated from,

$$\lambda_e \approx 3(K_c / \sigma_{hel})^2, \quad (16)$$

and, with a reasonable fracture toughness of  $K_c \approx 5$  MPa m<sup>1/2</sup>, provides  $\lambda_e \approx 0.3$   $\mu$ m. The two length scales clearly span the power-law distribution displayed in Figure (16) or (23).

Computational simulations of the time history of elastic strain accumulation in the impact event can be readily performed. The span of power-law fragmentation would be provided through the theory if a credible failure criterion can be applied within the computational model.

A failure criterion that has achieved some success in the fracture of brittle solids, as well as other critical state phenomena, is that attributed to Tuler and Butcher (1968). The Tuler-Butcher failure criterion can be expressed in the integral form,

$$I_{TB} = \int (\sigma(t) - \sigma_{th})^m dt \leq K_m. \quad (17)$$

The stress applicable to the applied loading conditions is  $\sigma$ , while  $\sigma_{th}$  is a corresponding threshold value of the stress. Failure occurs when the time-dependent Tuler-Butcher integral achieves the material constant  $K_m$ . The exponent  $m$  is a property of the material. For  $m=1$ , Equation (17) provides an impulse criterion, whereas for  $m=2$  the same equation is an energy or work criterion. As  $m$  becomes large Equation (17) approaches a constant stress failure criterion. When fit to experimental data an exponent  $m$  close to two is frequently observed. Impact breach tests on plates of soda-lime glass of Sun *et al.* (2006), for example, are described by a Tuler-Butcher failure criterion with  $m \approx 2$  for the Tuler-Butcher index [Grady, 2008]. The Tuler-Butcher criterion is appropriate for analytic models of ballistic failure where the stress within the integral is a sensible average over the elastic strain energy contribution to the catastrophic fragmentation [Grady, 2008]. The Tuler-Butcher criterion also has application in computational simulation.

### *Fragmentation Intensity Number*

In the theory of hydrodynamic turbulence the magnitude of the Reynolds number provides a measure of the extent of the inertial range – the span of length scales encompassing the entry level system scale powering the hydrodynamics, down to the limiting substructure scale necessary for the viscous dissipation. A similar dimensionless number characterizing the self-similar power-law range of the fragmentation event can be constructed by the ratio of the limiting correlation and energy length scale,

$$F = \lambda_c / \lambda_e . \quad (18)$$

If the kinematic state of the body leading to failure can be characterized by a single strain rate  $\dot{\epsilon}$ , then the limiting correlation length  $\lambda_c$  and the stress at failure of the body are related through,

$$\sigma = \rho c \dot{\epsilon} \lambda_c . \quad (19)$$

The energy limiting lower-bound length scale  $\lambda_e$  is related to the failure stress through,

$$\frac{\sigma^2}{2\rho c^2} = \frac{3\Gamma}{\lambda_e} , \quad (20)$$

where  $\Gamma$  is the fracture surface energy. Solving for  $F = \lambda_c / \lambda_e$  yields,

$$F = \frac{\sigma^3}{6\Gamma \rho^2 c^3 \dot{\epsilon}} . \quad (21)$$

In a complex body (a projectile impacting a brittle plate for example)  $\sigma$  provides a stress measure of the stored elastic strain energy at the onset of failure. For fragmentation intensity number  $F$  in the neighborhood of unity the stress can be solved for,

$$\sigma = \left( 6\Gamma \rho^2 c^3 \dot{\epsilon} \right)^{1/3} . \quad (22)$$

This is the failure stress under conditions of equilibrium fragmentation. The intensity number increases rapidly with stress as failure criteria in excess of equilibrium are achieved.

### *Correlation Horizon*

The concept of a correlation horizon [Grady, 1988] and the meaning of this correlation within the present context of dynamic fragmentation is worthy of additional thought. Consider the thin-walled spherical shell of metal as representative of the model depicted in Figure (21). The model assumes abrupt impulsive loading up to a uniform outward velocity  $V$ . In principle this initial requirement is physically reasonable. A step pressure of magnitude  $P = \rho c V$  could be applied uniformly over the inner surface of the shell. A shock

would propagate through the thickness  $d$  of the shell, reflect from the free surface and return a release wave. If the step pressure is maintained for a time  $2d/c$ , the impulse conditions sought are achieved. (Elastic-plastic behavior is ignored in this discussion.)

As outward motion proceeds, a uniform circumferential tension increases with time; the stress underlying the strain energy of Equation (11). In a continuum first-order assessment this time-dependent tension is independent of position throughout the body. Stress correlation plays a role in all real materials in that the modulus of elasticity is a function of circumferential position about the shell. Any number of practical reasons can be responsible for this position dependence. The fluctuation with position would be quite subtle in a glass material for instance. It would be markedly more pronounced in other engineering materials. Thus, the correlation of circumferential stress is time dependent and determined by the elastic wave speed. A weakest point (in the sense of fracture activation) in the body within a given correlation horizon may not necessarily be the weakest point at a lower loading rate where the correlation horizon is correspondingly larger.

The necessity of a correlation distance, and a corresponding correlation time, is evident in the direct imaging of impact fracture and fragmentation experiments on glass and ceramic plates of Straussberger *et al.* (2008). In those tests, the failure-induced stress wave is observed to propagate radially outward from the point of impact well ahead of any observed onset of fracture damage. These data are a clear example of the need for time-dependent stress correlation and concentration at preferred sites in the body to bring about brittle fracture and fragmentation.

### *Power-Law Fragmentation*

Fundamental physics demands that the fragment size distribution within the range of the two bounding length scales  $\lambda_e$  and  $\lambda_c$ , and sufficiently removed from either, be a power-law function of the fragment size. This physics is, of course, based on the proposed continuum fragmentation theory and the absence of any further intervening physical length scales. The same physics does not constrain the power-law exponent, however. Assessment of the exponent requires other physics be brought to bear.

The power-law nature of fragment size distributions resulting from the breakage of brittle solids has been noted by many since early in the last century, and probably earlier. Empirical evidence place the exponent  $n$  in the Schuhmann relation  $M(x) \propto x^n$  within the range of about  $0.5 < n < 1.5$ , with some applications achieving values approaching two and perhaps somewhat higher. There are studies in which values of  $n$  remarkably close to unity are observed [Bergstrom *et al.*, 1961]. A number of the earlier studies invoked the random placement of fracture flaws (a Poisson process) and some random geometric partitioning of the body. Notable are the theoretical efforts of Gaudin (1926), Bennett (1936), Lienau (1936) and Gilvarry (1961).

An intriguing alternative theoretical effort within this time frame was explored by Griffith (1943). He suggested an energy argument in which a specific energy  $\varepsilon \sim \gamma/\rho x$  is associated with a fragment of size  $x$ . The fracture surface energy and specific density are  $\gamma$

and  $\rho$ , respectively. He then invoked classical statistical mechanics to arrive at a Boltzmann representation of the fragment size distribution. In the large fragment limit a power-law distribution with  $n=1$  is achieved. Arguments are also offered for distribution in which  $n \neq 1$ .

Turcotti (1986) has pursued the fragmentation of brittle solids as a fractal process leading to  $N \sim x^{-d}$ , or correspondingly to  $M \sim x^n = x^{3-d}$ , relating the exponent  $n$  to the fractal dimension  $d$ . Turcotti explored group renormalization methods used by others to characterize various scale invariant critical state phenomena. He identifies a parameter  $p_m$  that determines the probability of fracturing of a cell of the solid body. The fractal dimension  $d$  is calculated from  $p_m$ , which he in turn relates to the fragility of the brittle material.

### Status of Brittle Fragmentation Theory

A theory of the dynamic fragmentation of solids based on continuum energy principles has provided a basis for assessing fragmentation in a wide range of ballistic applications over the past several decades. Applications of the theory to the fragmentation of brittle solids including glass and ceramic have been problematic. Recently, some of the physics issues governing length scales and sized distributions in the dynamic fragmentation of brittle solids have become known. The earlier equilibrium energy-based fragmentation theory is broadened to accommodate dynamic fragmentation in brittle materials.

The principal conclusion to this point is that a previous continuum energy-based fragmentation theory has application to both equilibrium (principally ductile materials) and nonequilibrium (brittle materials) fragmentation. The latter application, however, requires an additional failure criterion that is, at present, not well understood.

### *Fragmentation in Edge-On Plate Impact*

Experimental studies of Strassburger *et al.*, (2008) involving the edge-on impact of glass plates have provided experimental visualization of onset and advance of fracture failure. In this work, compact steel projectiles in either spherical or cylindrical geometry impact the edge of glass plates with thicknesses of approximately 10 mm. Impact causes elastic stress waves that propagate outward. Fracture failure of the plates follows behind the wave at a speed markedly less than the elastic wave velocity. High-speed shadowgraphs and photoelasticity are used to image the progression of failure. An illustration from the report of Strassburger *et al.*, [2008] shown in Figure (24) describes the experimental procedure. This experimental study is explored here with the emerging time-dependent failure and nonequilibrium fragmentation described in the previous sections and an earlier report [Grady, 2008]. Complexities in the impact loading and the subsequent wave propagation make this configuration more appropriately addressed by computational simulation. The test method is nonetheless examined here with approximate analytic techniques.

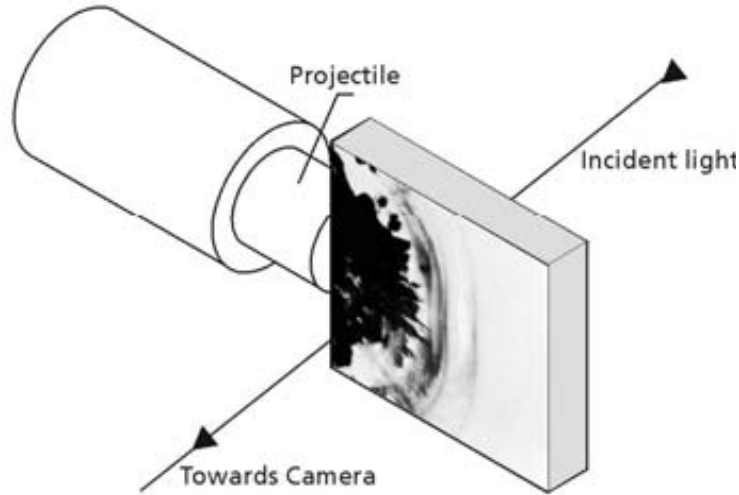


Figure 24: Illustration of the Edge-On impact failure experiments. The illustration is from the report of Strassburger *et al.*, [2008].

## Modelling the Impact Failure Event

Features of the edge-on impact failure experiment pertinent to the model are illustrated in Figure (25). In the region defined as the near field, impact-induced intense shock loading and large inelastic deformation combine to determine the extent of energy and momentum coupled to the plate. The mechanics in this region is difficult to address through either computational or analytic methods and is circumvented in the analysis to follow. An elastic stress wave will emerge from the near field region and propagate outward from the point of impact. This elastic wave will attenuate due to the cylindrical nature of the divergent wave propagation. Strain energy in this attenuating stress wave will be sufficient to cause failure through brittle fracture. Wave propagation and fracture failure in this far field region will be the subject of the present analysis.

An elastic stress pulse as a function of the radius from the impact point and time will be assumed of the form,

$$\sigma(r, t) = \sigma_o(r) e^{-t/\tau(r)}, \quad (23)$$

where the pre-exponential is provided by  $\sigma_o(r) = \sigma_o (r/a)^{-1/2}$  and accounts for the cylindrical attenuation of the peak shock stress. The length scale  $a$  is the distance at which the elastic pulse emerges from the near field and is of the order of the plate thickness. The time constant  $\tau(r)$  is a measure of the pulse width at a distance  $r$ . Let  $x = r/a$  be a dimensionless measure of the range and write,

$$\sigma(x, t) = \sigma_o x^{-1/2} e^{-t/\tau(x)}. \quad (24)$$

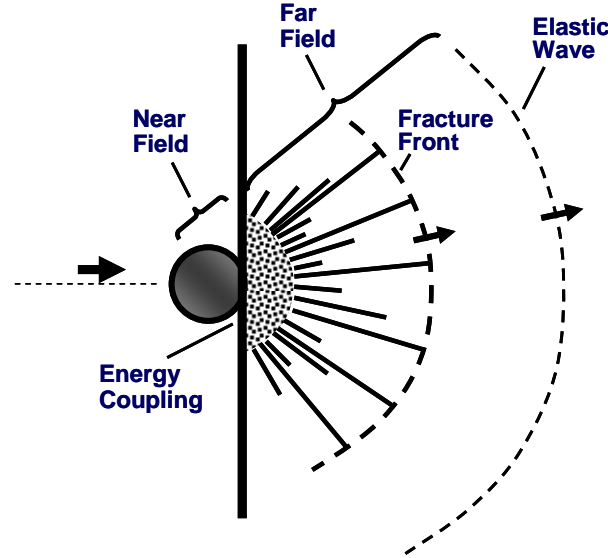


Figure 25: Features of impact failure and wave propagation in the Edge-On impact failure experiment.

In the far field, the impulse imparted by the elastic wave is sensibly constant if the elastic pulse is reasonably compact ( $c\tau(x) < x$  with  $c$  the elastic wave speed). A constant impulse in the elastic wave with propagation distance is assumed, although recognized as an over simplification of the wave propagation. Using Equation (24), the impulse in the wave is provided by,

$$\int_0^{\infty} \sigma(x, t) dt = \sigma(x) \tau(x) = \sigma_o \tau_o, \quad (25)$$

where time initiates at pulse arrival, and the second inequality follows from the initial peak stress and pulse duration on emerging from the near field region. A constant impulse requires that the wave pulse duration increase with propagation distance according to,

$$\tau(x) = \tau_o x^{1/2}. \quad (26)$$

Onset of fracture at some distance from impact is assumed to be governed by a time-dependent criterion of the Tuler-Butcher type written as,

$$\int_0^t \sigma^2 dt \leq \Gamma_{tb}. \quad (27)$$

Onset of failure through brittle fracture occurs when the integral achieves the value of the Tuler-Butcher energy  $\Gamma_{tb}$  (energy per unit area). Carrying out the integral in Equation (27) yields,

$$\frac{\sigma_o^2 \tau_o}{2\rho c} x^{-1/2} \left(1 - e^{-2t/\tau_o x^{1/2}}\right) = \Gamma_{tb}, \quad (28)$$

and provides an expression for the distance versus time path corresponding to fracture failure onset through the assumed time-dependent fracture criterion.

Equation (28) is rewritten as,

$$t(x) = -\frac{1}{2} \tau_o x^{1/2} \ln(1 - R x^{1/2}), \quad (29)$$

where,

$$R = \frac{2\rho c \Gamma_{tb}}{\sigma_o^2 \tau_o}, \quad (30)$$

provides a dimensionless measure of the ratio of the Tuler-Butcher failure energy to the input stress energy imparted by the impact.

The path of time-dependent brittle fracture failure provided by Equation (29) is governed by two parameters. The first is the energy ratio  $R$  provided through Equation (30). Second, is the characteristic pulse duration  $\tau_o$  of the input elastic stress pulse.

Qualitative predictions of the path of the fracture front based on Equation (29) are shown in Figure (26). An estimate of  $\tau_o = 6 \mu\text{s}$  for the pulse duration is based on a double elastic transit through a steel projectile of the dimensions used in the study of Strassburger *et al.*, [2008]. Values of the energy ratio of  $R = 0.2$  and  $R = 0.5$  are assumed, with the former value corresponding to the more intense impact energy. Fracture front paths are compared the longitudinal shock velocity of the exponential elastic stress pulse. The two calculations reveal that the path of the fracture front resides increasingly closer to the shock velocity as the impact energy is increased.

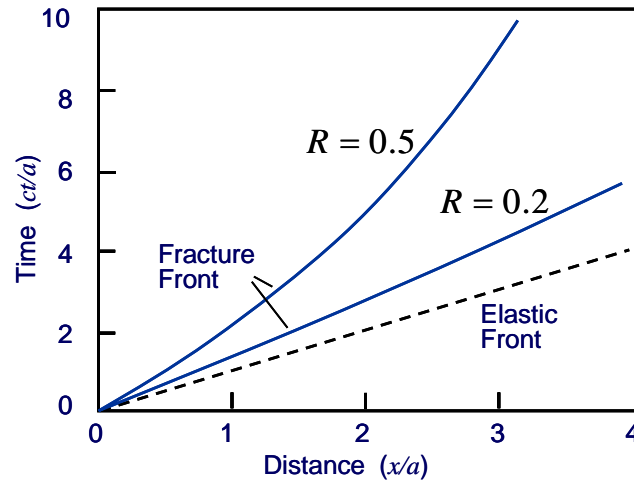


Figure 26: Features of impact failure and wave propagation in the edge-on impact failure experiment.

## Comparisons with Impact Failure

Experimental results from the edge-on impact of steel projectiles onto soda-lime silica glass [Strassburger *et al.*, 2008] are shown in Figure (27). Consecutive images of the fracture front are revealed by the diagnostic technique. Experimental assessment of the fracture front and the elastic wave front are provided in the plots. (Note that time is plotted on the abscissa in Figure (27) in contrast to the predictions in Figure (26)). A cylindrical projectile for the images on the left, and a spherical projectile for those on the right provided impact loading. Impact for both tests was at a comparable velocity. The cylinder would be expected to couple substantially more strain energy into the plate than would the sphere. This difference is borne out by the differences in the proximity of the fracture wave to the elastic wave for the two tests and is qualitatively consistent with the theory.

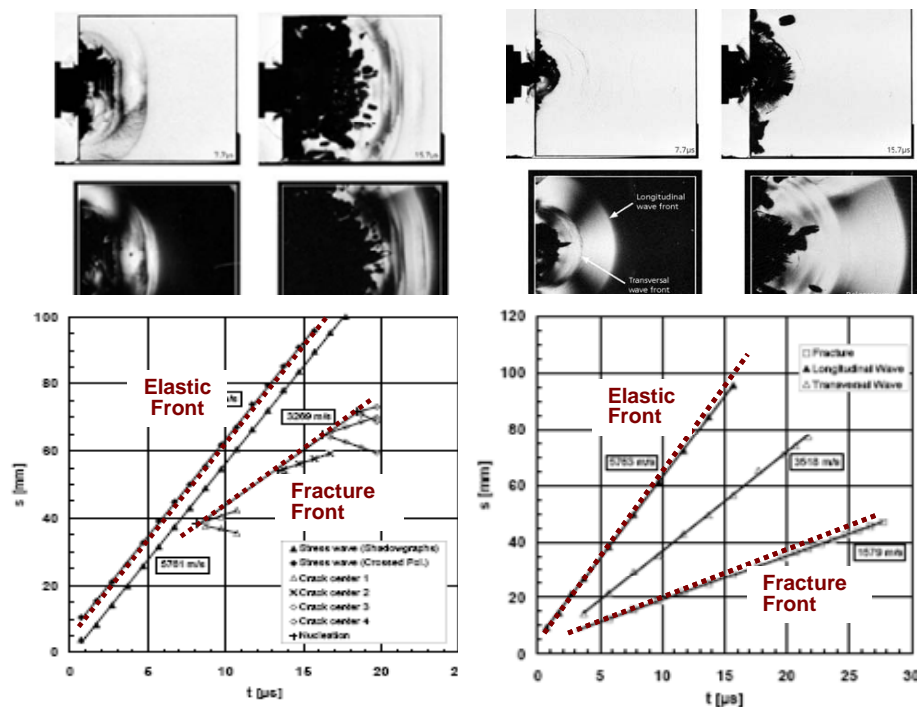


Figure 27: Images of fracture front at successive times in the edge-on impact of soda-lime silica glass subject to steel projectile impact at comparable velocities. Cylindrical projectile on the left. Spherical projectile on the right. Experimental estimates of elastic wave front and fracture front are shown in the plots [Strassburger *et al.*, 2008].

In Figure (28) a qualitative prediction is shown for the fragment distribution bounds resulting from brittle fracture at a specified distance from the point of impact based on time-dependent failure and an exponential history of the elastic strain energy history at the same point. This distribution would be a function of the propagation distance and would change (become coarser) with attenuation of the stress wave.



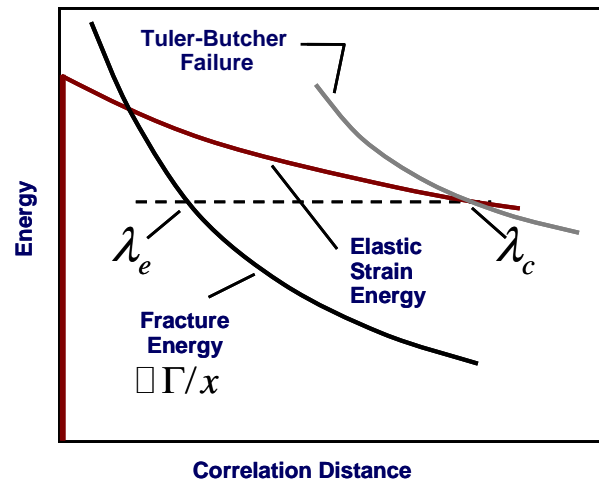


Figure 28: A qualitative prediction of the brittle fragment distribution at any distance from the point of impact based on a time-dependent failure criterion and the exponential strain energy history at the same distance.



## VI Closure and Conclusions

Shock wave data for both tungsten carbide and boron carbide are surveyed and used to assess hydrodynamic equation-of-state and dynamic strength properties of the two ceramics. This assessment is augmented with recent high-pressure ultrasonic and diamond anvil cell x-ray diffraction data for the former, and static size-scaling strength data for the latter.

Disparities between the high-pressure ultrasonic data and x-ray diffraction data, and their relationship to the experimental shock Hugoniot for tungsten carbide, initiated a critical assessment of the static tests and their dependencies on key microstructure properties of the test material. A physical model of nonhydrostatic stress states developed in the diamond anvil cell testing of hard materials suggest strength offset comparable to shock Hugoniot measurements. This prediction of near overlay of diamond anvil cell data and Hugoniot data is experimentally observed for tungsten carbide.

Large-anvil high-pressure ultrasonic methods to 14 GPa offer a promising technique for assessing high-pressure equation-of-state properties of ceramics. Assessment of the recent data on WC and WC-6%Co, however, indicates that careful attention to material microstructure is necessary in interpretation of the equation-of-state. Compressibility properties for WC appear affected by initial porosity and/or impurities in the ceramic tested, and extrapolation to high pressure is suspect. Properties for WC-6%Co are also influenced by microstructure in terms of influence of the differential compressibility of the WC and Co components. Using the data in conjunction with appropriate mixture models, however, provide promising results. Near convergence of the WC-6%Co data extrapolated to high pressure, when corrected for the cobalt component, with hydro compressibility of WC determined from shock Hugoniot data, provides improved confidence in the hydrodynamic equation of state for tungsten carbide.

Past analysis of boron carbide are brought together to provide a best assessment of the dynamic hydrodynamic equation of state of this ceramic. Both shock Hugoniot and high-pressure ultrasonic data are used for this assessment. That hydrodynamic or near-hydrodynamic conditions are achieved at high pressure is supported by the overlay of shock data on both near-full-density and porous boron carbide ceramic. Shock temperatures achieved in the latter approach melt. Evidence for two phase transformations over the range of study is prominently revealed by both shock and high-pressure static measurements. Dynamic strength of boron carbide remains enigmatic. Studies by different authors on different boron carbide ceramics provide markedly different evidence regarding dynamic strength.

Recent size scale studies of strength of boron carbide ceramic through indentation hardness measurements are compared with shock wave strength measurements. Size scale in the shock wave is established by the wave risetime over which strength and failure is tested. Agreement between the dynamic (shock) and static strength dependence on size scale supports arguments for time dependent strength and failure in the dynamic deformation of this ceramic.

Theoretical modeling of statistical fragmentation in the ballistic environment continues to improve. A feature emphasized in the present development relates to the marked differences in fragment size distributions resulting from ballistic events in both ductile and brittle solids. Fragment size distributions for ductile materials are exponential or near-exponential in functional form and constrained by a single size scale. In contrast, fragmentation in brittle solids results in power-law distributions and two physical size scales that bound the fragment size distribution. Governing length scales in the fragmentation process are calculated through the theory from physical properties of the materials, and energetic of the impact event. Work remains, however, in establishing failure criteria for brittle materials. Predictions of the power-law fragment distribution parameters are dependent on the failure criterion.

## VII References

1. Amulele, G. M., Manghnani, M. H., Marriappan, S., Hong, X., Li, F., Qin, X., Liermann, H. P., (2008) Compression behavior of WC and WC-6%Co up to 50 GPa Determined by Synchrotron X-Ray Diffraction and Ultrasonic Technique, *J. Appl. Phys.*, 103, 1.
2. Barrenblatt, G. I. (2006) Scaling Phenomena in Fatigue and Fracture, *Int. J. Fracture*, 138, 19-35.
3. Bennett, J. G. (1936) Broken Coal, *J. Inst. Fuel*, 10, 22-39.
4. Bergstrom, H. C., C.L. Sollenberger, W. Mitchel (1961) Energy Aspects of Single Particle Crushing, *Trans. AIME*, 220, 367-372.
5. Chhabildas, L., W. Reinhart, L. T. Wilson, D. R. Reedal, D. E. Grady and J. W. Black (2001) Fragmentation Properties of AerMet 100 Steel in Two Material Conditions, *Proceedings 19th International Symposium on Ballistics*, Interlaken, Switzerland, I.R. Crewther, ed., 663-670, May 7-11.
6. Curran, D. R., L. Seaman, D.A. Shockey (1987) Dynamic Failure of Solids, *Physics Repts.*, 147, 253-288.
7. Dandekar, D. P., (2001) Shock Response of Boron Carbide, Army Research Laboratory Report ARL-TR-2456, April.
8. Dandekar, D. P. and Bartkowski, P.T., (2001) Tensile Strengths of Silicon Carbide under Shock Loading, Army Research Laboratory Report ARL-TR-2430, March.
9. Dandekar D. P. and Grady D. E., (2002) Shock Equation of State and Dynamic Strength of Tungsten Carbide, *Shock Compression of Condensed Matter–2001*, edited by M Furnish, N Thadhani and Y Horie, American Institute of Physics, 783-786.
10. Falkovich, G. and K.R. Sreenivasan (2006) Lessons from Hydrodynamic Turbulence, *Physics Today*, 59, 4, 43-49.
11. Gaudin, A. M. (1926) Investigation of Crushing Phenomena, *AIME Trans.*, 73, 253-316.
12. Gilvarry, J. J. (1961) Fracture of Brittle Solids. I. Distribution Function for Fragment Size in Single Fracture (Theoretical), *J. Appl. Phys.*, 32, 391-399.
13. Grady, D. E. (1982) Local Inertial Effects in Dynamic Fragmentation, *J. Appl. Phys.*, 53, 322-325.
14. Grady, D. E. (1988) The Spall Strength of Condensed Matter, *J. Mech. Phys. Solids*, 36, 3, 353-384.
15. Grady, D. E. (1990) Particle Size Statistics in Dynamic Fragmentation, *J. Appl. Phys.* 68, 12, 6099-6105.
16. Grady, D. E., (1994) Shock Wave Strength Properties of Boron Carbide and Silicon Carbide, *International Conference on Mechanical and Physical Behavior of Materials under Dynamic Loading*, les Editions de Physique, pp. 385-391.

17. Grady, D. E. (1995) Dynamic Properties of Ceramic Materials, Sandia National Laboratories Technical Report, SAND94-3266, February.
18. Grady, D. E., (1999) Impact Failure and Fragmentation Properties of Tungsten Carbide, *Int. J. Impact Engng.* 23, 307-317.
19. Grady, D. E., (2002), Analysis of Shock and High-Rate Data for Ceramics: Application to Boron Carbide and Silicon Carbide, Applied Research Associates Rept., for U.S. Army TACOM-TARDEC, August.
20. Grady, D. E., (2003) Analysis of Shock and High-Rate Data for Ceramics: Equation of State Properties, Applied Research Associates Rept., for U.S. Army TACOM-TARDEC, December.
21. Grady, D. E. (2006) Fragmentation of Rings and Shells, Springer.
22. Grady, D. E. (2008) Fragment Size Distributions from the Dynamic Fragmentation of Brittle Solids, *Int. J. Impact Engng.*, 35, 1557-1562.
23. Grady, D. E. (2008) Analysis of Shock and High-Rate Data for Ceramics: Failure and Fragmentation in the Shock and Ballistic Environment, Prepared for, U.S. Army TACOM-TARDEC, *Applied Research Associates Tech. Rept.*, April.
24. Grady, D. E. (2009) Dynamic Fragmentation of Solids, in Shock Waves Science and Technology Reference Library Vol. 3, Y. Horie, ed.
25. Grady, D. E. and Doolittle, C., (2001 Preliminary Compressibility Analysis of Boron Carbide from High-Pressure Shock and Ultrasonic Data, Applied Research Associates Rept., for U.S. Army TACOM-TARDEC, February.
26. Grady, D. E., C.A. Hall, W.D. Reinhart (1996) Sandia National Laboratories Technical Memorandum, unpublished.
27. Grady, D.E. and Moody, R. L. (1996), Shock Compression Profiles in Ceramics, Sandia National Laboratories Technical Report, SAND96-0551, March, 1996.
28. Griffith, L. (1943) A Theory of the Size Distribution of Particles in a Comminuted System, *Canadian Journal of Research*, 21A, 6, 57-64.
29. Gust, W. H., and Royce, E. B., (1971) Dynamic Yield Strength of B<sub>4</sub>C, BeO and Al<sub>2</sub>O<sub>3</sub> Ceramics, *J. Appl. Phys.*, 42, 276.
30. Kirkland, T. P., Wereszczak, A. A., Strong, K. T., Jadaan, O. M., Thompson, G. A., (2009) Strength-Size Scaling Response of Boron Carbide over a Wide Range of Effective Areas, Poster Presentation, 33<sup>rd</sup> Int. Conf. of Advanced Ceramics and Composites: Symposium on Armor Ceramics, Daytona Beach, FL, January 18-23.
31. Lienau, C. C. (1936) Random Fracture of a Brittle Solid, *J. Franklin Inst.*, 221, 485-494, 674-686, 769-787.
32. Manghnani, M. H., (2007) Private Communication.
33. Manghnani, M. H., Wang, Y., Zinin, F., and Rafaniello, W., (2000) Elastic and Vibrational Properties of B<sub>4</sub>C to 21 GPa., Science and Technology of High Pressure

- Volume 2, Proc. Int. Conf. on High Pressure Science and Technology (AIRAPT-17), July 25–30, University Press, p. 945–948.
34. Marsh, S. P., (1980) LASL Shock Hugoniot Data, Edited by SP Marsh, University of California Press, Berkeley.
  35. McQueen, R. G., Marsh, S. P., Taylor, J. W., Fritz J. N., Carter, W. J., (1970) The Equation of State of Solids from Shock Wave Studies, In High Velocity Impact Phenomena, R Kinslow ed., Academic Press.
  36. Mott, N. F. (1943) A Theory of the Fragmentation of Shells and Bombs, *United Kingdom Ministry of Supply* AC4035, May.
  37. Mott, N. F. (1947) Fragmentation of Shell Cases, *Proc. Royal Soc.*, A189, 300-308, January.
  38. Mott, N. F. and E.H. Linfoot (1943) A Theory of Fragmentation, *United Kingdom Ministry of Supply* AC3348, February.
  39. Moynihan, T. J., J.C. LaSalvia, M.S. Burkins (2002) Analysis of Shatter Gap Phenomenon in a Boron Carbide/Composite Laminate Armor System, *Proc. Int. Ballistics Symp.*, Sept..
  40. Schuhmann, R. (1940) Principles of Comminution, I., Size Distribution and Surface Calculations, AIME Tech. Publ. 1189, *Mining Technology*, 1-11.
  41. Shockey, D. A., L. Seaman, D.R. Curran (1973) in Metallurgical Effects at High Strain Rates, R.W. Rohde *et al.*, eds., Plenum.
  42. Straussberg, E., P. Parimal, J.W. McCauley, C. Kovalchick, K.T. Ramesh, D.W. Templeton (2008) High-Speed Transmission Shadowgraphic and Dynamic Photoelasticity Study, *Army Research Laboratory Rept.*, ARL-RP-203, March.
  43. Sun, X. M., A. Khaleel, R.W. Davies (2006) Modeling of Stone-Impact Resistance of Monolithic Glass Ply Using Continuum Damage Mechanics, *Int. J. Damage Mech*, 14, 165-178.
  44. Swegle, J. W. and Grady, D. E. (1985), Shock Viscosity and the Prediction of Shock Wave Rise Times, *J. Appl. Phys.*, 58 (2), 692-701.
  45. Tuler, F. R. and B.M. Butcher (1968) A Criterion for the Time Dependence of Fracture, *Int. J. Fracture Mech.*, 4, 431-437.
  46. Turcotte, D. L. (1986) Fractals and Fragmentation, *J. Geophys. Res.*, 91, 1921-1926.
  47. Vogler, T. J., Reinhart, W.D., Chhabildas, L. C., (2004) Dynamic Behavior of Boron Carbide, *J. Appl. Phys.*, 95, 8, 4173.
  48. Vogler, T. J., Lee, M.Y., Grady, D. E., (2007) Static and Dynamic Compaction of Ceramic Powders, *Int. J. Solids Structures*, 636-658.
  49. Wereszczak, A.A., Kirkland T.P., Strong, K.T. Jr., Jadaan, O.M. and Thompson, G.A., (2009) Size-Scaling of Tensile Failure Stress in Boron Carbide, *Advances in Applied Ceramics: Structural, Functional and Bioceramics* (in Press).

50. Zhang, Y., Mashimo, T., Uemura, Y., Uchino, M., Kodama, M., Shibata, K., Fukuoka, K., Kikuchi, M., Kobayashi, T., Sekine, T. (2006) Shock Compression Behaviors of Boron Carbide, *J. Appl. Phys.* 100, 113536.